UC Irvine
Faculty Publications

Title
Global Modeling Initiative assessment model: Model description, integration, and testing of the transport shell

Permalink
https://escholarship.org/uc/item/4hw6q2cb

Journal
Journal of Geophysical Research, 106(D2)

ISSN
0148-0227

Authors
Rotman, D. A
Tannahill, J. R
Kinnison, D. E
et al.

Publication Date
2001

DOI
10.1029/2000JD900463

Copyright Information
This work is made available under the terms of a Creative Commons Attribution License, availalbe at https://creativecommons.org/licenses/by/4.0/

Peer reviewed

eScholarship.org Powered by the California Digital Library
University of California

JOURNAL OF GEOPHYSICAL RESEARCH, VOL. 106, NO. D2, PAGES 1669–1691, JANUARY 27, 2001

Global Modeling Initiative assessment model: Model description, integration, and testing of the transport shell

D. A. Rotman,[1] J. R. Tannahill,[1] D. E. Kinnison,[1,2] P. S. Connell,[1] D. Bergmann,[1] D. Proctor,[1] J. M. Rodriguez,[3] S. J. Lin,[4] R. B. Rood,[4] M. J. Prather,[5] P. J. Rasch,[2] D. B. Considine,[6] R. Ramaroson,[7] and S. R. Kawa[4]

Abstract. We describe the three-dimensional global stratospheric chemistry model developed under the NASA Global Modeling Initiative (GMI) to assess the possible environmental consequences from the emissions of a fleet of proposed high-speed civil transport aircraft. This model was developed through a unique collaboration of the members of the GMI team. Team members provided computational modules representing various physical and chemical processes, and analysis of simulation results through extensive comparison to observation. The team members' modules were integrated within a computational framework that allowed transportability and simulations on massively parallel computers. A unique aspect of this model framework is the ability to interchange and intercompare different submodules to assess the sensitivity of numerical algorithms and model assumptions to simulation results. In this paper, we discuss the important attributes of the GMI effort and describe the GMI model computational framework and the numerical modules representing physical and chemical processes. As an application of the concept, we illustrate an analysis of the impact of advection algorithms on the dispersion of a NO_y-like source in the stratosphere which mimics that of a fleet of commercial supersonic transports (high-speed civil transport (HSCT)) flying between 17 and 20 km.

1. Introduction

1.1. Previous Assessment Activities

The Atmospheric Effects of Stratospheric Aircraft (AESA) component of the National Aeronautics and Space Administration (NASA) High Speed Research Program (HSRP) sought to assess the impact of a fleet of high-speed civil transport (HSCT) aircraft on the lower stratosphere. There are several components to such an assessment. Laboratory and field measurements, characterization of the exhaust products, and development of realistic scenarios for the distribution of emissions all play important roles. Models integrate information from the above efforts to calculate the fate of aircraft exhaust, the buildup of such pollution in the lower stratosphere, and the model response of ozone to the change in lower stratospheric composition. The use of models is thus a key element of the assessment, as models are the primary tools through which the impact on the ozone layer is quantified.

[1]Lawrence Livermore National Laboratory, Livermore, California.
[2]National Center for Atmospheric Research, Boulder, Colorado.
[3]Department of Marine and Atmospheric Chemistry, University of Miami, Miami, Florida.
[4]NASA Goddard Space Flight Center, Greenbelt, Maryland.
[5]Department of Earth System Science, University of California at Irvine.
[6]Department of Meteorology, University of Maryland, College Park.
[7]Office National d'Etudes et Recherches Aerospatiales, Chatillon, France.

Copyright 2000 by the American Geophysical Union.

Paper number 2000JD900463.
0148-0227/00/2000JD900463$09.00

Previous assessments of the impact of anthropogenic emissions on the stratosphere have relied primarily on two-dimensional (2-D) models where the stratosphere's variability along a latitude circle is ignored [*Prather et al.*, 1992; *Stolarski et al.*, 1995; *Kawa et al.*, 1999; *World Meteorological Organization (WMO)*, 1999; *Intergovernmental Panel on Climate Change (IPCC)*, 1999]. The theoretical foundations for such an approach were laid out in a series of studies resulting in the development of the concepts of a residual circulation and eddy mixing. These approximations allowed extracting the residual effects of the cancellation between reversible and irreversible transport by mean winds and planetary waves averaged over a latitude circle [*Andrews and McIntyre*, 1976; *Dunkerton*, 1978]. Model refinements have yielded calculated distributions of stratospheric species, particularly ozone, which have reproduced the general features of the observed spatial and temporal distribution of column ozone. Furthermore, the first application of these models to the assessment of the impact of fluorocarbons emitted at the surface capitalized on the zonal symmetry of the problem, since these emissions were zonally well-mixed upon arrival at the tropical tropopause. Lastly, these models allowed multiyear calculations necessary for assessment efforts, and consideration of an increasing number of different emission scenarios as the efficiency of computational platforms has increased.

1.2. Need for Three-Dimensional Models

As has been pointed out from the start of AESA [*Douglass et al.*, 1991], that many aspects of aircraft exhaust perturbations on ozone are more appropriately modeled in three dimensions. The aircraft are proposed to fly mainly in the Northern Hemisphere and always over the oceans with a high concentration of

flight paths in identifiable oceanic corridors. Thus the pollutant source is zonally asymmetric and concentrated in a geographical region. The meteorology of the Northern Hemisphere stratosphere is influenced by the land ocean pattern, thus the transport of polluted air from the stratosphere to the troposphere is also asymmetric. There have been efforts to evaluate the importance of these asymmetries to the assessment calculation, and to quantify expected differences from a two-dimensional calculation [*Douglass et al.*, 1993; *Rasch et al.*, 1994; *Weaver et al.*, 1995, 1996]. Although these studies all suggest fairly small impacts to the buildup of exhaust for three-dimensional (3-D) (versus two-dimensional (2-D)) models; the National Research Council Panel on the AESA reviewed the NASA Interim Assessment [*Albritton et al.*, 1993] and recommended the use of three-dimensional models to evaluate the uncertainties associated with transport [*Graedel*, 1994].

Results from laboratory kinetics and observations also point to the three-dimensionality of stratospheric processes. Formation of polar stratospheric clouds (PSCs) and heterogeneous reactions on these particles are extremely sensitive to local values of temperature, pressure, and concentrations of nitric acid, water, and sulfuric acid [*Solomon et al.*, 1986; *Hofmann and Solomon*, 1989; *WMO*, 1999]. These induce zonal asymmetries in chemistry which are poorly represented in two-dimensional models.

There are fundamental advantages to a three-dimensional representation of the atmosphere which includes state-of-the-art formulations of stratospheric chemical and transport processes which are not well represented in two-dimensional models. These processes include (but are not limited to) the wave mean flow interaction, the seasonal and geographic variation in the tropopause height, the representation of cross tropopause transport at a synoptic scale, the seasonal evolution of the polar vortices, and the asymmetric behavior of PSC formation and chlorine activation at high latitudes. The 3-D models improve the physical basis for representing these processes. In some cases, comparisons of models with observations reflect these improvements. For example, the amplitude of the annual cycle in total ozone at northern middle latitudes is generally closer to the observed amplitude in 3-D models than in 2-D models [*Rasch et al.*, 1995; *Douglass et al.*, 1997]. The improved agreement is at least partially a result of a more physical representation of the tropopause and the concomitant transport in the lowermost stratosphere. Thus both the nature of the problem of assessing HSCT impacts, and the specific processes to be included, point to the need to develop three-dimensional assessment tools. Moreover, future assessments of aircraft will include subsonic aircraft requiring the inclusion of tropospheric chemical, physical, and dynamical processes. Such studies will certainly require the use of 3-D global models, thus experience gained in the application of 3-D models to stratospheric assessments will accelerate progress in the troposphere.

However, it should also be pointed out that advancing to a three-dimensional model does not automatically provide a perfect solution nor provide a solution to all assessment needs. A major disadvantage of 3-D models for assessment is their large computational requirements. Since the motivation for using the 3-D model rests on the improved physical basis of the model, the horizontal and vertical resolution must be adequate to resolve important transport processes. The transport and photochemical time steps must both be substantially smaller than the time steps often used in 2-D models. It is important to remember that 2-D models have long been used to calculate constituent evolution, and comparisons of calculated fields with zonal means of global observations has been a principal means of evaluating the 2-D models [e.g., *Prather and Remsberg*, 1993]. As noted above, 2-D model transport has a strong theoretical basis, but retains a strong phenomenological component underlying simplifying assumptions and parameterizations. The 3-D models do not have this heritage for constituent modeling; hence it is likely that for some constituents, 2-D models may still give equal or better comparison to observations. However, improvement in the representation of physical processes inherent in 3-D models sets the stage for physically based improvements in these models, often through interpretation of the differences between model fields and constituent observations. Ultimately, these improvements of a more realistic representation will yield a better assessment tool and reduce the uncertainties in the predicted impact of HSCTs, a goal of the AESA program.

2. GMI Philosophy

The large computational needs of 3-D chemical transport models (CTMs) along with the large need in human resources to develop, maintain, and apply the models combine to allow fewer independent groups to carry out 3-D chemistry simulations. Moreover, many times the design of the model is closely tied to the available data in the input meteorological data. These situations (and others) preclude the comprehensive clean intercomparison of individual model components. This problem exists even for two-dimensional models and is amplified for three-dimensional models. Model evaluation against observations also becomes a larger task, requiring both computational and human resources. It is thus impractical that 3-D assessments follow the path of 2-D assessments, in which independent calculations were produced by several research groups. To gain the benefits of using the 3-D assessment and maintain involvement of several research groups, the Global Modeling Initiative (GMI) science team was formed. The goal of this group is to produce a well tested and evaluated 3-D chemistry and transport model that is useful for assessment calculations. In order to incorporate efficiently ongoing improvement in model components, and facilitate analysis and evaluation, a modular design has been adopted. This design allows various numerical transport schemes, photochemical schemes, and sets of meteorological data (winds and temperatures) to be tested within a common framework [*Thompson et al.*, 1996]. Such a framework is very useful for understanding sensitivities and uncertainties in assessment simulations by swapping in and out particular numerical schemes and evaluating impacts on simulation results. In addition, the framework is maintained under strict software engineering practices making use of version control and coding standards to enable portability and usability.

3. GMI Science Team

Science team members were selected to provide either modules for inclusion into the GMI model or data/analysis for GMI model evaluation. The current GMI Science Team is shown in Table 1. Participation of key scientists in both integration and analysis sets the stage for conceptual development. This development involves the creation of a computing infrastructure that enables the careful assessment of the influence of various chemical, physical, and dynamical modules to stratospheric

Table 1. GMI Science Team Members, Institution, and Their Contribution to the GMI Model Development, Evaluation, and Application[a]

PI	Co-I	Institution	Contribution
Brasseur	Hess, Lamarque	NCAR	stratospheric chemistry module and analysis of influence of stratosphere-troposphere exchange to aircraft impacts
Rasch		NCAR	CCM2 meteorological data sets and semi-Lagrangian transport algorithms
Rood	Coy, Lin	NASA Goddard	DAO assimilated data and the flux form semi-Lagrangian transport algorithm
Douglass	Kawa, Jackman	NASA Goddard	model evaluation against satellite, aircraft, and surface data; photolysis lookup table; cold sulfate and polar stratospheric cloud parameterizations
Considine		NASA GSFC and University of Maryland	PSC parameterization
Hansen, Rind		NASA GISS	NASA GISS II′ meteorological data sets
Prather		University of California, Irvine	second-order moment transport algorithm; CTM model diagnostics; mass tendencies diagnostics and module
Ko	Weisenstein	AER Corporation	2-D model simulation and analysis and aerosol surface area density fields for input to assessment simulations
Pickering	Allen	University of Maryland	NO_x lightning parameterization
Jacob	Logan, Spivakosy	Harvard University	tropospheric chemistry module; tropospheric chemistry mechanism; emission database; and ozone climatology for model evaluation
Penner		University of Michigan	parameterization of lightning NO_x, and aerosol microphysical model
Geller	Yudin	SUNY, Stony Brook	integration of 3-D meteorological data into 2-D model framework for analysis of transport fields
Baughcum, Wuebbles		Boeing Company and University of Illinois	high-speed civil transport emission scenarios and characterization
Ramaroson		ONERA, France	stratospheric chemistry module
Isaksen		University of Oslo	ECMWF meteorological data analysis
McConnell		York University	York University CTM results and analysis
Visconti		University of L'Aquila	aerosol microphysics
Tennenbaum		SUNY, Purchase	aircraft meteorological data input toward improvement of assimilation products
Walcek	Milford	SUNY, Albany	convection and deposition algorithms
Kinnison		LLNL	stratospheric chemistry module; radionuclide simulations and analysis
Rotman	Tannahill, Bergmann, Connell	LLNL	model infrastructure and implementation of science modules

[a]PI, principal investigator; Co-I, co-investigator.

chemistry simulations, in particular to those assessing the influence of aircraft emissions on ozone. The infrastructure is designed such that individual modules can be swapped in and out providing both an understanding of the influence of those modules as well as an understanding of the uncertainty and sensitivity of simulations to those modules. Members of the science team played a crucial role in evaluating the scientific performance of the model by extensive comparison to observations. These evaluations are discussed in detail by *Douglass et al.* [1999] and J. M. Rodriguez et al. (manuscript in preparation, 2000). In the next section we provide details of the GMI assessment modules and computing framework. Then we provide a transport simulation showing how such a modular computing structure including multiple transport algorithms can be used to improve the understanding of transport uncertainties in aircraft assessments.

4. Description of the GMI Model

In this section we will describe the modules that make up the GMI assessment model, paying particular attention to those modules having multiple options. These modules represent input meteorological data, advection algorithms, mass tendencies, numerical schemes for chemistry solutions, the chemistry mechanism, heterogeneous processes, photolysis, diagnostics, treatment of tropospheric processes, and initial and boundary conditions. Table 2 summarizes these algorithms and options and shows those options selected for use in assessment simulations enclosed in parentheses.

4.1. Meteorological Input Data

The GMI model incorporates three different sets of input meteorological data: two from general circulation model (GCM) outputs, the National Center for Atmospheric Research (NCAR) Middle Atmospheric Version of the Community Climate Model, Version 2 (MACCM2) and the Goddard Institute for Space Studies (GISS) Model II′, and one set of GEOS-Stratospheric Tracers of Atmospheric Transport (STRAT) assimilated data representing 1996 from the NASA Data Assimilation Office. Data from all these input sets included horizontal U and V winds, temperature, and surface pressure. Below, we give details of sources for these meteorological fields.

4.1.1. Data Assimilation Office (DAO) assimilated meteorological fields. NASA Data Assimilation Office at Goddard has provided data sets from the GEOS-STRAT assimilation system. All data are 6-hour time-averaged and were an interpolated product from the original 2° by 2.5° by 46 level DAO output to a 4° by 5° by 29 level. These fields represent the years of May 1995 through May 1996. The top of the data set is 0.1 hPa. The vertical structure is 11 sigma layers below 130 hPa and 18 log pressure levels above 130 hPa. Data were provided at cell centers (commonly referred to as A grid).

Table 2. Summary Table of GMI Algorithms and Model Data

Module	Options
Input meteorological data	NASA Data Assimilation Office (DAO) assimilated fields
	(NCAR MACCM2 GCM fields)
	NASA GISS II′ GCM fields
Advection algorithm	semi-Lagrangian transport (SLT)
	(flux form semi-Lagrangian transport (FFSLT))
	second-order moments (SOM)
Mass tendencies	(NASA GISS/University of California, Irvine, pressure filter (pdyn0))
Numerical schemes for chemistry solutions	SMVGEAR II
	(semi-implicit symmetric method (SIS))
Chemistry mechanism	(GMI stratospheric mechanism (see text for details))
Heterogeneous processes	(University of Maryland cold sulfate and polar stratospheric cloud parameterization)
Photolysis	(GSFC lookup table)
Diagnostics	(University of California, Irvine, module-based species tendencies)
Tropospheric treatment	(simplified wet scavenging of species)
Initial conditions	(combined observations and GSFC 2-D model output)
Boundary conditions	(source gases [*WMO*, 1994, Table 6-3; *Stolarski et al.*, 1995])
	(water vapor from GSFC 2-D and UARS MLS)
	(SAGE surface area density of aerosols)

4.1.2. NCAR MACCM2 GCM meteorological fields. NCAR provided 1 year's worth of output from their MACCM2 using conditions representing mid-1990s. This output is provided on a 64 by 64 Gaussian grid, which approximates 3° by 6° horizontal resolution. The top of the model is 0.025 hPa with fields provided on 44 levels. For use in the GMI model this data were interpolated to a regular 4° by 5° horizontal mesh. The vertical structure of this output is in a hybrid sigma-pressure coordinate system, which represents a smooth transition between mainly sigma in the troposphere and nearly log pressure in the stratosphere. The data represent cell-centered (A grid) 6-hour-averaged MACCM2 output.

4.1.3. GISS II GCM meteorological fields. NASA GISS has provided 1-year output from their GISS II′ GCM using conditions representative of the 1990s. This data were provided through the University of California, Irvine. This output uses a 4° by 5° horizontal grid with 28 layers to 0.02 mbar. The vertical structure of this data is 11 sigma layers below 100 mbar and 17 log pressure layers above 100 mbar. Six-hour-averaged data are provided on cell centers for state variables and cell edges for mass fluxes (commonly referred to as C grid).

4.1.4. Vertical resolution of input meteorological data. As will be discussed later in the paper, an important feature of the input meteorological data is its vertical resolution. Vertical resolution in the lower stratosphere is especially important to aircraft assessment simulations because of the sharp vertical definition of the emissions. Within the region of aircraft emissions (18 to 20 km) these data sets possess vertical resolutions of the following: DAO GEOS-STRAT, ~1.0 km; NCAR MACCM2, ~1.4 km; GISS II′, ~3 km.

4.2. Advection

The GMI model contains three advection algorithms to transport trace species. These three schemes are the semi-Lagrangian transport scheme of *Rasch and Williamson* [1991], the second-order moment method of *Prather* [1986], and the flux form semi-Lagrangian (FFSL) algorithm of *Lin and Rood* [1996]. Extensive validation simulations were carried out to ensure proper implementation. The availability of different advection schemes has enabled the evaluation of the influence of advection numerics on simulation results. Tracer simulations relevant to aircraft impact studies were carried out using differing advection schemes and/or differing meteorological data. Results show important ramifications to assessment results from details on the design of the advection numerics. Details and simulation results are given later in the paper.

4.2.1. Semi-Lagrangian transport (SLT). The transport of tracer species is done using a three-dimensional shape-preserving semi-Lagrangian transport formalism. The transport scheme was originally developed for the transport of water vapor in the troposphere [*Rasch and Williamson*, 1991]. More recently, it has been used for the simulation of stratospheric aerosol transport [*Boville et al.*, 1991], the transport of radioactive isotopes [*Rasch et al.*, 1994], and the transport of CFCs in troposphere [*Hartley et al.*, 1994]. The shape-preserving attributes of this transport algorithm can maintain very sharp gradients without introducing overshoots or undershoots and diffuses only at the smallest scales of the model. The semi-Lagrangian transport is not inherently conservative, and a mass correction, which we term a "mass fixer," must be applied to the solution at the end of each time step to strictly enforce this conservation [*Rasch et al.*, 1995]. Because the original semi-Lagrangian transport algorithms were developed for water vapor, we have encountered a number of minor problems in their use in transporting species in the middle atmosphere. Minor modifications have been made to the algorithms to make them more appropriate for the transport of trace species. Briefly, we have modified the transport algorithm to move trace species mixing ratios normalized by dry air mass rather than the original formulation which used mixing ratios normalized by moist air mass.

4.2.2. Second-order moment (SOM). The second-order moments (SOM) algorithm for tracer transport [*Prather*, 1986] is derived from the slopes scheme [*Russell and Lerner*, 1981]. It conserves tracer mass, is positive definite, only moves tracers by explicitly resolved mass flows, and has been demonstrated to have extremely high accuracy in a wide variety of three-dimensional tests. The method stores and transports moments of the tracer distribution in three dimensions. Within each grid box the tracer mass mixing ratio is described by a second-order polynomial in (x, y, z) that is decomposed into 10 orthogonal polynomials in $\{1, x, y, z, x2, y2, z2, xy, xz, yz\}$. The coefficient of each polynomial is the "moment" value. The SOM is an upstream advection algorithm. The amount of mass

from the upstream box is "cut off" and moved into the downstream box where the two different polynomial distributions are then combined (addition/conservation of moments is equivalent to least squares fitting to the polynomials). One advantage of storing the tracer distribution (instead of recalculating it each step) is that advection involves only the immediate upstream/downstream boxes and does not require neighboring points to fit polynomials. The algorithm works on the background "mass" of the boxes and thus has no problems with operator splitting in flow fields where mass can accumulate during intermediate steps. The accuracy of the method is based in part on its storage of nine additional quantities beyond just the mean amount of tracer. These additional memory requirements, however, are only equivalent to doubling the resolution in three dimensions (factor of 8) and still give better accuracy. In atmospheric modeling, the chemistry and emission patterns are often mapped onto and directly interact with the higher-order moments. The SOM scheme in its original form (1986) has the disadvantage that it generates anomalous ripples near sharp gradients. We have included options to the original scheme which reduce these ripples.

4.2.3. Flux form semi-Lagrangian transport (FFSLT). The third advection scheme is the flux form semi-Lagrangian transport (FFSLT) algorithm of *Lin and Rood* [1996]. This scheme is a multidimensional algorithm that explicitly considers the fluxes associated with cross terms to enable the use of one-dimensional schemes as the basic building block. These one-dimensional operators are based on high-order Godunov-type finite volume schemes (primarily third-order piecewise parabolic method (PPM)). The algorithm is upstream in nature to reduce phase errors and contains multiple monotonicity constraints to eliminate the need for a filling algorithm and the severe problems that would arise with negative values of chemical species concentrations. These constraints act to constrain subgrid tracer distributions. This scheme also avoids the strict Courant stability problem at the poles, thus allowing large time steps to be used, resulting in a highly efficient advection.

The algorithm uses two-dimensional horizontal winds from input meteorological data to derive vertical mass fluxes from conservation of mass and the hydrostatic continuity equation. Fluxes at the model top and surface are identically zero. The model can incorporate pure sigma, pure log pressure, or any combination sigma and log pressure as vertical coordinates.

Simulation results from the NASA Models and Measurements II exercise [*Park et al.*, 1999] showed this algorithm to have an optimal combination of low diffusion, conservation, and computational performance; hence the FFSLT was selected for work described in this paper. Details of these simulations are shown in section 6.

4.3. Mass Tendencies

In models describing the meteorological fields, that is, the climate or assimilation models from which GMI derives its meteorological fields, the surface pressure varies according to the convergence of total mass by the wind fields. In most of these models, however, there are discrepancies between the pressure tendency and the column convergence of mass due to mass redistribution that is not explicitly resolved by the winds (e.g., Shapiro filtering of surface pressure). Other possible sources for these discrepancies are numerical differences between the equation for the pressure tendency and the derived mass fluxes used by chemistry models or possibly, simply, the use of time-averaged fields where the averaging may have impacted the close relationship between pressure tendency and column convergence. When chemistry models use the meteorological fields, the column air mass will deviate from the surface pressure predicted by the climate/assimilation model, and this difference, $P(\mathrm{CTM}) - P(\mathrm{met\ field})$, is designated as the pressure error $P(\mathrm{err})$. All known chemistry models have this problem, even those running "on-line."

A simple fix that most chemistry models adopt is merely to reset the surface pressure to that of the meteorological field every 6 to 24 hours. In doing this, the air mass in the column is abruptly changed, usually by a few tenths of a percent (i.e., a few hPa). The chemistry model designer has the option of conserving the tracer mass (in which case the error correction induces errors in the tracer mixing ratio of similar magnitude) or conserving mixing ratio (in which case the tracer mass develops similar magnitude errors). If the pressure errors are small, then the former fix is usually adopted and is not apparent as an error, and the induced variability is swamped by the rest of the processes in the chemistry model. Nevertheless this resetting of the surface pressure does create "source/sink-like" terms in the tracer and can induce upward/downward flow across sigma surfaces. Since the GMI model transports species as volume mixing ratio, variations in the total mass of the atmosphere will necessarily yield variations in the total burden of atmospheric chemical species. Such variations could influence interpretation of simulation results.

A simple fix to the $P(\mathrm{err})$ problem has been implemented in GMI. The key is to generate a resolved (u, v) wind field that corrects the $P(\mathrm{err})$ by a resolved mass flow that carries tracer with it, thus conserving total tracer mass and mixing ratio. A pressure filter maintains the CTM and meteorological field surface pressures separately. For each new met field (e.g., every 3 hours) the projected $P(\mathrm{CTM})$ is compared with the $P(\mathrm{met})$ to generate a $P(\mathrm{err})$. The $P(\mathrm{err})$ is then filtered to generate a (u, v)-corrected wind field that when added to the original (u, v) field, greatly reduces (but does not entirely eliminate) $P(\mathrm{err})$. (An exact Laplace solution eliminating $P(\mathrm{err})$ is possible, but not worth the computational effort.) In this way the $P(\mathrm{CTM})$ field is different from $P(\mathrm{met})$, yet follows the $P(\mathrm{met})$ field for multiyear simulations [*Prather et al.*, 1987].

4.4. Numerical Schemes for Chemistry Solutions

4.4.1. SMVGEAR II. SMVGEAR II [*Jacobson*, 1995] is a technique capable of highly accurate solutions to both stiff and nonstiff sets of ordinary differential equations. SMVGEAR II is a version of the original predictor/corrector, backward differentiation code of *Gear* [1967] and uses a variable time step, variable-order, implicit technique for solving stiff numerical systems with strict error control. The chemical continuity equation is solved for each individual species (i.e., no lumping of species into chemical families are made). SMVGEAR II, as designed for large vector supercomputers, separates the grid domain into blocks of grid cells, each containing approximately 500 grid cells (large vector lengths are optimal). The cells in each block are reordered for stiffness (see *Jacobson* [1995] for details) and solved. In GMI model simulations using massively parallel computers (more information on parallel computing is in following sections) we found that reducing the block size from 500 to around 60–80 produced a 20% gain in speed with no loss of accuracy. With its high accuracy, SMVGEAR II was used as a benchmark to assess the accuracy of other chemistry solution techniques.

4.4.2. ONERA-SIS. The semi-implicit symmetric (SIS) method was developed, numerically analyzed, and applied for various atmospheric models by *Ramaroson* [1989]. It was developed to include chemical tendencies in an operator split GCM (currently, the EMERAUDE model of METEO FRANCE [*Ramaroson*, 1989; *Ramaroson et al.*, 1991, 1992a, 1992b; *Chipperfield et al.*, 1993] and is also used in the MEDIANTE 3-D chemical transport model [*Sausen et al.*, 1995; *Claveau and Ramaroson*, 1996] and box models calculations [*Ramaroson et al.*, 1992a]. The method has also been applied to combustion chemistry and aqueous phase within clouds. The SIS method is more precise than explicit and implicit Euler solutions. However, when compared to the Gear's method (like SMVGEAR II), SIS is less precise near sunset and sunrise only where SMVGEAR uses a higher-order expansion and a very small time step (see discussion in section 6).

4.5. Chemistry Mechanism

The GMI model includes a mechanism focused on stratospheric chemistry with simplified tropospheric chemistry (i.e., methane). The mechanism includes photolysis and reactions of species in the species families O_x, NO_y, ClO_y, HO_y, BrO_y, CH_4, and its oxidation products. The chemical mechanism includes 46 transported species, 116 thermal reactions, and 38 photolytic reactions. Source gases present in the model include N_2O, CH_4, CO_2, CO, the chlorine-containing compounds CFC-11, -12, -113, -114, -115, HCFC-22, CCl_4, CH_3CCl_3, and CH_3Cl, and the bromine-containing compounds CH_3Br, CF_2ClBr, and CF_3Br (see Table 3). Absorption cross section information was assembled from a variety of sources, including Jet Propulsion Laboratory (JPL) Publication 97-4. Most of the thermal reaction rate constants were taken from *DeMore et al.* [1997], the NASA Panel recommendations provided in JPL Publication 97-4.

In simulations used to compare directly to observed data, the model did include the $ClO + OH \rightarrow HOCl$ reaction; however, in assessment simulations of aircraft in 2015 this reaction was not included. This was done to remain more consistent with the 2-D models which also carried out assessment simulations. A detailed treatment of heterogeneous processes on both sulfate and ice aerosols are included within this mechanism [*Considine et al.*, 2000].

4.6. Heterogeneous Processes

The GMI model includes a parameterization of polar stratospheric clouds (PSC) that will respond to increases in HNO_3 and H_2O produced, for example, by aircraft emissions. Both type 1 and type 2 PSCs are considered. The parameterization also accounts for PSC sedimentation, which can produce denitrification and dehydration at the poles. The GMI PSC parameterization is designed to be economical, so it does not represent the microphysical processes governing PSC behavior. Here we describe the basics of the parameterization; more details on this module are given by *Considine et al.* [2000].

The parameterization calculates surface area densities (SAD) for type 1 and type 2 PSCs using model-calculated temperatures and HNO_3 concentrations, aircraft emitted water vapor as well as background H_2O distributions, the ambient pressure, and an H_2SO_4 concentration which is inferred from the background liquid binary sulfate (LBS) aerosol distribution specified in the model calculation. The type 1 PSC calculation can be set to assume either a nitric acid trihydrate (NAT) or a STS composition (it is currently set to STS). The assumed composition of the type 2 PSCs is water ice. The vapor pressure measurements of *Hanson and Mauersberger* [1988] are used for NAT PSCs; the approach of *Carslaw et al.* [1995] is used for the STS composition; and *Marti and Mauersberger* [1993] vapor pressures are used for ice aerosols. The code removes both H_2O and HNO_3 from gas to condensed phase when particles form. To calculate the amount of material removed from gas phase, the parameterization assumes thermodynamic equilibrium. When ice PSCs form, the algorithm assumes that a coexisting NAT phase also forms and is part of the type 2 PSC. This provides a mechanism for significant denitrification of the polar stratosphere due to rapid sedimentation of the large type 2 PSCs. A user-specified threshold supersaturation ratio for both NAT and ice aerosols must be exceeded before any mass is removed from the gas phase. Current values for these ratios correspond to a 3 K supercooling for NAT aerosols and a 2 K supercooling for ice aerosols, consistent with the estimates of *Peter et al.* [1991] and *Tabazadeh et al.* [1997].

In order to calculate the surface area density corresponding to a particular amount of condensed phase mass, the code assumes the condensed phase mass to obey a lognormal particle size distribution. The user can specify either the total particle number density and the distribution width, or the particle median radius and the distribution width, which then determines the conversion from condensed phase mass to surface area density. When the particle number density is held constant, condensation or evaporation processes result in the growth or shrinkage of existing particles rather than new particle nucleation. This is thought to be more physically realistic.

The parameterization transports the condensed phase H_2O and HNO_3 vertically to account for particle sedimentation. The condensed phase constituents are also subject to transport by the model wind fields. Fall velocities are calculated according to *Kasten* [1968] and corrected to account for the range of fall velocities in a lognormally distributed ensemble of aerosol particles. This correction factor can be important [see *Considine et al.*, 2000]. Because the GMI model currently specifies the background distribution of H_2O in the stratosphere, a special strategy had to be developed to allow for dehydration resulting from particles sedimentation. This takes the form of a special transported constituent (named "dehyd") which is produced when dehydration occurs due to particle sedimentation and is lost when moistening of a region results from local evaporation of particles sedimenting from higher altitudes. Ambient H_2O concentrations are then the difference between the background H_2O and "dehyd."

It should be stressed that this parameterization is not microphysical. A comprehensive microphysical representation of PSCs would be computationally expensive and so is not appropriate in a model designed for assessment calculations.

4.7. Photolysis

Photolysis rates are obtained by a clear-sky lookup table [*Douglass et al.*, 1997]. Normalized radiative fluxes calculated from the model of *Anderson et al.* [1995] are tabulated as a function of wavelength, solar zenith angle, overhead ozone, and pressure. Temperature-dependent molecular cross sections, quantum yields, and solar flux are tabulated separately. In the GMI model, fluxes and cross sections are interpolated to the appropriate values for each grid and integrated over wavelength to produce photolysis rates. This method compares well to the photolysis benchmark intercomparisons [*Stolarski et al.*, 1995]. Photolysis rates are obtained using a uniform global

Table 3. Detailed Description of the GMI Chemical Mechanism, Reactions, and Rates

	Kinetic Parameters					Notes
	A			E/R		a
	k_0^{300}	n	k_∞^{300}	m	B	b
Reactions						
$O + O_2 + M = O_3$	6.0e-34	2. 3.	0.	0.		c
$O + O_3 = 2\ O_2$	8.0e-12			2060.		c
$O(^1D) + N_2 = O + N_2$	1.8e-11			−110.		c
$O(^1D) + O_2 = O + O_2$	3.2e-11			−70.		c
$O(^1D) + O_3 = 2\ O_2$	1.2e-10			0.		c
$O(^1D) + H_2O = 2\ OH$	2.2e-10			0.		c
$O(^1D) + H_2 = OH + H$	1.1e-10			0.		c
$O(^1D) + N_2O = N_2 + O_2$	4.9e-11			0.		c
$O(^1D) + N_2O = 2\ NO$	6.7e-11			0.		c
$O(^1D) + CH_4 = CH3O_2 + OH$	1.125e-10			0.		c
$O(^1D) + CH_4 = CH_2O + H + HO_2$	3.0e-11			0.		c
$O(^1D) + CH_4 = CH_2O + H_2$	7.5e-12			0.		c (branching ratio, JPL note A9)
$O(^1D) + CF_2Cl_2 = 2\ Cl$	1.20e-10			0.		c (JPL notes A2 and A15)
$O(^1D) + CFC113 = 3\ Cl$	1.50e-10			0.		c (JPL note A15)
$O(^1D) + HCFC22 = Cl$	7.20e-11			0.		c (JPL notes A15 and A23)
$H + O_2 + M = HO_2$	5.7e-32	1.6	7.5e-11	0.		c
$H + O_3 = OH + O_2$	1.4e-10			470.		c
$H_2 + OH = H_2O + H$	5.5e-12			2000.		c
$OH + O_3 = HO_2 + O_2$	1.6e-12			940.		c
$OH + O = O_2 + H$	2.2e-11			−120.		c
$OH + OH = H_2O + O$	4.2e-12			240.		c
$HO_2 + O = OH + O_2$	3.0e-11			−200.		c
$HO_2 + O_3 = OH + 2\ O_2$	1.1e-14			500.		c
$HO_2 + H = 2\ OH$	7.0e-11			0.		c (products, JPL note B5)
$HO_2 + OH = H_2O + O_2$	4.8e-11			−250.		c
$HO_2 + HO_2 = H_2O_2 + O_2$						d
$HO_2 + HO_2 + H_2O = H_2O_2 + O_2 + H_2O$						e
$H_2O_2 + OH = H_2O + HO_2$	2.9e-12			160.		c
$N + O_2 = NO + O$	1.5e-11			3600.		c
$N + NO = N_2 + O$	2.1e-11			−100.		c
$NO + O_3 = NO_2 + O_2$	2.0e-12			1400.		c
$NO_2 + OH + M = HNO_3$	2.32e-30	2.97	1.45e-11	2.77		f
$NO + HO_2 = NO_2 + OH$	3.5e-12			−250.		c
$NO_2 + O = NO + O_2$	5.26e-12			−209.		g
$NO_2 + O_3 = NO_3 + O_2$	1.2e-13			2450.		c
$NO_2 + HO_2 + M = HO_2NO_2$	1.8e-31	3.2	4.7e-12	1.4		c
$NO_3 + O = O_2 + NO_2$	1.0e-11			0.		c
$NO_3 + NO = 2\ NO_2$	1.5e-11			−170.		c
$NO_3 + NO_2 + M = N_2O_5$	2.2e-30	3.9	1.5e-12	0.7		c
$N_2O_5 + M = NO_2 + NO_3$	8.15e-04	3.9	5.56e+14	0.7	11000.	c
$HNO_3 + OH = H_2O + NO_3$						c (see expression in reference)
$HO_2NO_2 + M = HO_2 + NO_2$	8.57e-05	3.2	2.24e+15	1.4	10900.	c
$HO_2NO_2 + OH = H_2O + NO_2 + O_2$	1.3e-12			−380.		c (products assumed)
$Cl + O_3 = ClO + O_2$	2.9e-11			260.		c
$Cl + H_2 = HCl + H$	3.7e-11			2300.		c
$Cl + H_2O_2 = HCl + HO_2$	1.1e-11			980.		c
$Cl + HO_2 = HCl + O_2$	1.8e-11			−170.		c
$Cl + HO_2 = OH + ClO$	4.1e-11			450.		c
$ClO + O = Cl + O_2$	3.0e-11			−70.0		c
$ClO + OH = HO_2 + Cl$	1.1e-11			−120.		k from c, see h for branching ratio
$ClO + OH = HCl + O_2$	1.1e-11			−120.		k from c, see h for branching ratio
$ClO + HO_2 = O_2 + HOCl$	4.8e-13			−700.		c (branching ratio, JPL note F43)
$ClO + HO_2 = O_3 + HCl$	0.0e-00			0.		c (branching ratio, JPL note F43)
$ClO + NO = NO_2 + Cl$	6.4e-12			−290.		c
$ClO + NO_2 + M = ClONO_2$	1.8e-31	3.4	1.5e-11	1.9		c
$ClO + ClO = 2\ Cl + O_2$	3.0e-11			2450.		c
$ClO + ClO = Cl_2 + O_2$	1.0e-12			1590.		c
$ClO + ClO = Cl + OClO$	3.5e-13			1370.		c
$ClO + ClO + M = Cl_2O_2$	2.2e-32	3.1	3.5e-12	1.0		c
$Cl_2O_2 + M = 2\ ClO$	1.69e-05	3.1	2.69e+15	1.0	8744.	c
$HCl + OH = H_2O + Cl$	2.6e-12			350		c
$HOCl + OH = H_2O + ClO$	3.0e-12			500.		c
$ClONO_2 + O = ClO + NO_3$	4.5e-12			900.		i
$ClONO_2 + OH = HOCl + NO_3$	1.2e-12			330.		c (products assumed)
$ClONO_2 + Cl = Cl_2 + NO_3$	6.5e-12			−135.		c (products, JPL note F71)
$Br + O_3 = BrO + O_2$	1.7e-11			800.		c
$Br + HO_2 = HBr + O_2$	1.5e-11			600.		c

Table 3. (continued)

	Kinetic Parameters					Notes
	A			E/R		a
	k_0^{300}	n	k_∞^{300}	m	B	b
$Br + CH_2O = HBr + HO_2 + CO$	1.7e-11			800.		c
$BrO + O = Br + O_2$	1.9e-11			−230.		c
$BrO + HO_2 = HOBr + O_2$	3.4e-12			−540.		c (products, JPL note G21)
$BrO + NO = Br + NO_2$	8.8e-12			−260.		c
$BrO + NO2 + M = BrONO_2$	5.2e-31	3.2	6.9e-12	2.9		c
$BrO + ClO = Br + OClO$	1.6e-12			−430.		c
$BrO + ClO = Br + Cl + O_2$	2.9e-12			−220.		c
$BrO + ClO = BrCl + O_2$	5.8e-13			−170.		c
$BrO + BrO = 2\ Br + O_2$	2.4e-12			−40.		c (branching ratio, JPL note G37)
$HBr + OH = Br + H_2O$	1.1e-11			0		c
$CO + OH = H + CO_2$						j
$CH_4 + OH = CH_3O_2 + H_2O$	2.45e-12			1775.		c
$CH_2O + OH = H_2O + HO_2 + CO$	1.0e-11			0.		c
$CH_2O + O = HO_2 + OH + CO$	3.4e-11			1600.		c
$Cl + CH_4 = CH_3O_2 + HCl$	1.1e-11			1400.		c
$Cl + CH_2O = HCl + HO_2 + CO$	8.1e-11			30.		c
$CH_3O_2 + NO = HO_2 + CH_2O + NO_2$	3.0e-12			−280.		c
$CH_3O_2 + HO_2 = CH_3OOH + O_2$	3.8e-13			−800.		c
$CH_3OOH + OH = CH_3O_2 + H_2O$	2.7e-12			−200.		c (branching ratio, JPL note D15)
$CH_3Cl + OH = Cl + H_2O + HO_2$	4.0e-12			1400.		c
$CH_3CCl_3 + OH = 3\ Cl + H_2O$	1.8e-12			1550.		c
$HCFC22 + OH = Cl + H_2O$	1.0e-12			1600.		c
$CH_3Cl + Cl = HO_2 + CO + 2\ HCl$	3.2e-11			1250.		c
$CH_3Br + OH = Br + H_2O + HO_2$	4.0e-12			1470.		c
$N_2O_5 + LBS = 2\ HNO_3$						k
$ClONO_2 + LBS = HOCl + HNO_3$						k
$BrONO_2 + LBS = HOBr + HNO_3$						k
$HCl + ClONO_2 = Cl_2 + HNO_3$						k
$HCl + HOCl = Cl_2 + H_2O$						k
$HOBr + HCl = BrCl + H_2O$						k
$N_2O5 + STS = 2\ HNO_3$						l
$ClONO_2 + STS = HOCl + HNO_3$						l
$BrONO2 + STS = HOBr + HNO_3$						l
$HCl + ClONO_2 = Cl_2 + HNO_3$						l
$HCl + HOCl = Cl_2 + H_2O$						l
$HOBr + HCl = BrCl + H_2O$						l
$ClONO_2 + NAT = HOCl + HNO_3$						m
$BrONO_2 + NAT = HOBr + HNO_3$						m
$HCl + ClONO_2 = Cl_2 + HNO_3$						m
$HCl + HOCl = Cl_2 + H_2O$						m
$HCl + BrONO_2 = BrCl + HNO_3$						m
$HOBr + HCl = BrCl + H_2O$						m
$ClONO_2 + ICE = HOCl + HNO_3$						n
$BrONO2 + ICE = HOBr + HNO_3$						n
$HCl + ClONO_2 = Cl_2 + HNO_3$						n
$HCl + HOCl = Cl_2 + H_2O$						n
$HCl + BrONO_2 = BrCl + HNO_3$						n
$HOBr + HCl = BrCl + H_2O$						n
$HNO_3 + SOOT = NO_2 + OH$						o
Reaction (photolysis process)						
$O_2 + h\nu = O + O$						
$O_3 + h\nu = O + O_2$						
$O_3 + h\nu = O(^1D) + O_2$						
$HO_2 + h\nu = OH + O$						
$H_2O_2 + h\nu = 2\ OH$						
$H_2O + h\nu = H + OH$						
$NO + h\nu = N + O$						
$NO_2 + h\nu = NO + O$						
$N_2O + h\nu = N_2 + O(^1D)$						
$NO_3 + h\nu = NO_2 + O$						
$NO_3 + h\nu = NO + O_2$						
$N_2O_5 + h\nu = NO_2 + NO_3$						
$HNO_3 + h\nu = OH + NO_2$						
$HO_2NO_2 + h\nu = OH + NO_3$						
$HO_2NO_2 + h\nu = HO_2 + NO_2$						
$Cl_2 + h\nu = 2\ Cl$						
$OClO + h\nu = O + ClO$						
$Cl_2O_2 + h\nu = 2\ Cl + O_2$						
$HOCl + h\nu = OH + Cl$						

Table 3. (continued)

	Kinetic Parameters					Notes
	A			E/R		a
	k_0^{300}	n	k_∞^{300}	m	B	b
Reaction (photolysis process)						
$ClONO_2 + h\nu = Cl + NO_3$						
$ClONO_2 + h\nu = ClO + NO_2$						
$BrCl + h\nu = Br + Cl$						
$BrO + h\nu = Br + O$						
$HOBr + h\nu = Br + OH$						
$BrONO_2 + h\nu = Br + NO_3$						
$BrONO_2 + h\nu = BrO + NO_2$						
$CH_3OOH + h\nu = CH_2O + HO_2 + OH$						
$CH_2O + h\nu = CO + H_2$						
$CH_2O + h\nu = HO_2 + CO + H$						
$CH_3Cl + h\nu = CH_3O_2 + Cl$						
$CCl_4 + h\nu = 4\ Cl$						
$CH_3CCl_3 + h\nu = 3\ Cl$						
$CFCl_3 + h\nu = 3\ Cl$						
$CF_2Cl_2 + h\nu = 2\ Cl$						
$CFC113 + h\nu = 3\ Cl$						
$CH_3Br + h\nu = Br + CH_3O_2$						
$CF_3Br + h\nu = Br$						
$CF_2ClBr + h\nu = Br + Cl$						

[a] $k = Ae^{-E/RT}$.
[b] $k = \{(k_0(T)[M])/(1 + k_0(T)[M]/k_\infty(T))\}0.6^{\{1+[\log_{10}(k_0(T)[M]/k_\infty(T))]^2\}^{-1}}e^{-B/T}$, $k_0(T) = k_0^{300}(T/300)^{-n}$, $k_\infty(T) = k_\infty^{300}(T/300)^{-m}$.
[c] *DeMore et al.* [1997].
[d] $k = 2.3 \times 10^{-13}e^{600/T} + 1.7 \times 10^{-33}[M]e^{1000/T}$.
[e] $k = (2.3 \times 10^{-13}e^{600/T} + 1.7 \times 10^{-33}[M]e^{1000/T})1.4 \times 10^{-21}e^{2200/T}$.
[f] *Brown et al.* [1999].
[g] *Gierczak et al.* [1999].
[h] *Lipson et al.* [1997]; branching ratio for HCl as product = $1.7 \times 10^{-13}e^{363/T}/4.2 \times 10^{-12}e^{280/T}$.
[i] *Goldfarb et al.* [1998].
[j] From reference in note c above; $k = 1.5 \times 10^{-13}(1.0 + 0.6P)$, P in atm.
[k] Heterogeneous surface reaction; LBS represents liquid binary sulfate aerosol surface area.
[l] Heterogeneous surface reaction; STS represents sulfate ternary solution aerosol surface area (PSC type I).
[m] Heterogeneous surface reaction; NAT represents nitric acid trihydrate aerosol surface area (alternate form of PSC type I).
[n] Heterogeneous surface reaction; ICE represents ice aerosol surface area (PSC type II).
[o] Heterogeneous surface reaction; SOOT represents carbonaceous aerosol surface area.

mean surface albedo of 0.3 and a cloud-free atmosphere. Cross sections and quantum yields are from *DeMore et al.* [1997].

4.8. Diagnostics

Diagnostics have been implemented in the GMI model to enable assessing total mass and the changes in species concentrations in each grid box caused by each operator (i.e., horizontal and vertical advection, chemistry, etc.). The diagnostic tracks concentrations before and after each module, and provides time-averaged information in one-dimensional (in altitude) or two-dimensional (in latitude and altitude) output. Such diagnostics are very useful in analyzing what processes control the distribution of chemical species in particular regions of the atmosphere.

4.9. Tropospheric Treatment and Transport

The chemical mechanism was focused primarily on quality and efficient stratospheric chemistry simulations. For wet scavenging, the model used a simple vertically dependent removal lifetime [*Logan*, 1983]. Near the ground the lifetime of wet-deposited species was assumed to be 1 day and increases to 38 days near the tropopause. Species deposited using this method are HNO_3, HCl, and $BrONO_2$. There are no surface emissions of chemical species, and the model does not include dry deposition, vertical diffusion, or convection schemes for tracer transport.

4.10. Initial and Boundary Conditions

Zonally averaged initial conditions for chemical species are obtained from the GSFC 2-D model. Boundary conditions for the source gases in the GSFC 2-D model were set as follows: evaluation/validation runs for comparison to observations used 1995 conditions from *WMO* [1994, Table 6-3], while aircraft assessment simulations representing 2015 used conditions described by *Stolarski et al.* [1995]. For these long-lived species the GMI model reset the bottom two model layers to the values obtained from initial conditions.

The GMI focused on stratospheric chemical processes important to HSCT assessments and did not attempt to predict the background distribution of water vapor related to complex tropospheric hydrologic processes. Instead, it incorporated water vapor fields obtained from an assimilation of MLS water vapor measurements into the GSFC 2-D model. To allow the polar stratospheric cloud parameterization to correctly represent polar processes such as dehydration, the background water vapor fields necessarily eliminated any dehydration as seen in MLS measurements. A regression algorithm involving CLAES N_2O measurements and MLS water vapor measure-

ments was used to fill dehydrated regions in the MLS observations. The resulting altered MLS water vapor distribution (from 80°S to 80°N, and from 70 hPa to 0.3 hPa) was used to constrain the GSFC 2-D model. In the troposphere, water vapor was further constrained by observations of *Oort* [1983]. Steady state 2-D water vapor fields were used as background in GMI simulations.

The GMI model used distributions of monthly averaged aerosol surface area densities for heterogeneous reactions on sulfate aerosols. For present-day simulations of the GMI model, we used SAGE-based surface area density data from *Thomason et al.* [1997] which described the background distribution of aerosols during the year of 1996. For the aircraft assessment we used the designated SA0 distribution representing a clean atmosphere as detailed by *WMO* [1992, Table 8-8]. In neither case did we attempt to include the sulfate aerosols created by the combustion process of aircraft fuels containing sulfur. Two-dimensional model simulations of aircraft effects show important perturbations caused by this additional source of sulfate aerosols [*Kawa et al.*, 1999; *IPCC*, 1999]. Future work with the GMI model will include these effects.

5. Parallelization and Computational Timings of GMI

Three-dimensional atmospheric chemistry models require large amounts of computer time and effort because of the complex nature of the modeling and the need to perform long simulations due to the long timescales of the stratosphere. To enable multiyear chemistry simulations, the GMI core model was parallelized to make use of the most powerful computational platforms available. An existing LLNL computational framework [*Mirin et al.*, 1994] was used to implement the GMI model on parallel computers. This framework uses a two-dimensional longitude/latitude domain decomposition whereby each subdomain consists of a number of contiguous columns having a full vertical extent. Processors are assigned to subdomains, and variables local to a given package/subdomain are stored on the memory of the assigned processor. Data are transmitted between computational processes, when needed, in the form of messages. The number of meshpoints per subdomain may be nonuniform, under the constraint that the decomposition be logically rectangular. The choice to decompose in only two dimensions is based on the fact that the chemistry, photolysis, and cold sulfate algorithms make up the vast majority of the computational requirements and are all either local or column calculations. Thus these computations require no communication with neighboring grid zones and hence maximize the parallel efficiency.

Because of the wide spectrum of architectures together with a typical computer lifetime of just a few years, it is important to maintain a portable source code. We have encountered two major issues that affect portability: message passing and dynamic memory management. To address these issues, we use the MPI message passing interface and FORTRAN90's dynamic memory capabilities. The GMI model runs on virtually all leading edge massively parallel processors, including the Cray-T3E, SGI Origin2000, and IBM-SP. The model also runs on clusters of workstations (IBM, SUN, COMPAQ/DEC), as well as on the Cray-C90 and J90 (multitasking was not implemented in the model, hence C90 and J90 simulations used one processor). Although portability is quite important, it is equally important to exploit each architecture as much as possible. Toward that end, the framework makes use of conditional compilation to allow inclusion of optimization constructs particular to given architectures. The parallel framework provides the domain decomposition functionality, the detailed aspects of the message passing, and a number of other useful utilities. Nearly all coding in the model is written in FORTRAN 77/90, with a small amount of C. This framework is the backbone of the GMI model. All submitted algorithms and modules have been incorporated into this structure. This two-dimensional decomposition does impose communication requirements in the east-west and north-south advection operator. The FFSLT scheme requires species information in the adjacent two cells in order to form the profiles of species distributions to establish the flux of species through cell edges. However, the unique capability of the FFSLT to accurately deal with high Courant number flows in the east-west direction near the poles was a special issue for parallelization. In that region of the grid the size of the grid zone becomes very small in the east-west direction, and to enable large time steps (i.e., Courant stability defined on the equatorial grid sizes), the Courant numbers near the pole become larger than 1. The algorithm accurately deals with these large Courant numbers in the polar region by changing its advection algorithm to one that possesses a Lagrangian (trajectory) character (here it shares many characteristics with traditional semi-Lagrangian methods, and hence its name of the flux form semi-Lagrangian scheme; see *Lin and Rood* [1996] for details of the implementation). With the possibility of Courant numbers much larger than one, we needed to ensure domains have species information at locations larger than two adjacent grid zones. For each subdomain we maintain "ghost cells" which represents the species information in the adjacent zones. Information in these ghost zones is exchanged between domains via message passing. The possibility of large Courant numbers in the polar regions forces the need for large numbers of ghost zones in the east-west direction, which increases the communication cost (and hence, decreases the parallel efficiency). As a compromise, we use four ghost zones in each direction and adjust the time step to ensure Courant numbers are never larger than four.

The parallelization effort has worked well to allow multiyear stratospheric chemistry simulations and has enabled the application of the GMI model to the assessment of stratospheric aircraft emissions [*Kawa et al.*, 1999; *Kinnison et al.*, this issue]. The breakdown of the CPU requirements on a Cray C90 for the GMI model is as follows: chemistry, 78%; advection, 12%; photolysis, 7%; cold sulfate/PSC, 3%. These values are approximate only and represent the breakdown on a C90 style large vector machine (see next section for more details). Given the communication costs of the advection scheme, on parallel machines the fraction of time spent there will be larger. However, in general, the local and column processes of chemistry, photolysis, and PSC/cold sulfate correspond to the majority of the computational needs and allow good parallel efficiency. Scaling is near linear when increasing processor numbers to about 100. Increasing above that level, we see about 70–80% efficiency. This makes sense since on a given problem, increasing the processor count decreases the number of grid zones in a domain, but the number of ghost zones required remains at four. Eventually, you reach a point where the number of ghost zones is larger than the number of zones in the computational domain, which acts to decrease the parallel efficiency. Nonetheless, the use of parallel computers allowed us to carry out

Table 4. Advection Algorithm Timings With a Single Tracer (No Chemistry)

Algorithm	Timing (C90 Seconds per Year per Grid Zone)
FFSLT	0.024
SLT	0.020
SOM	0.150

many more simulations than possible otherwise. The actual assessment simulations were done [see *Kinnison et al.*, this issue] using a grid resolution of 4° by 5° in the horizontal and 44 levels in the vertical. The total number of species was 51. On a Cray C90 a simulated year required approximately 308 hours to complete. The same problem, using 181 processors of a Cray T3E-600, required 35 hours. (Timings here represent CPU times.) We present a series of GMI model computer timings (all timings are CPU times) in Tables 4–8.

6. Scientific Performance of Numerical Solution to Chemistry

Two photochemical solvers, the Onera-SIS and SMVGEAR II solvers introduced above, were investigated as potential modules for the GMI assessment calculations. Solver derivations and numerics have been discussed above and in the cited references. In summary, the Onera-SIS solver is expected to be stable for photochemical time steps at or below 900 s, to conserve atomic abundances, and to be fast at third-order accuracy. The SMVGEAR II solver uses a variable-order technique with variable internal time steps, which allows longer operator time steps, if desired. SMVGEAR II is expected to produce a more accurate solution around terminator transients than Onera-SIS with its fixed time step. The additional computational cost of the SMVGEAR II technique as applied in GMI is shown in Tables 7 and 8.

Initial comparisons were made in box model simulations with initial conditions taken from multidimensional stratospheric model output. Thirty day simulations with 900 s time steps were conducted for the Onera-SIS and LSODE solvers. The LSODE solver is a relative and precursor of the SMVGEAR II solver, suitable for application in a single box. Photolysis frequencies were precalculated and held fixed during each time step. Figure 1a shows the absolute value of the percent difference in 24 hour average concentrations of the last day of simulation, representing mid-January at 48°N latitude and 20 km altitude, for Onera-SIS relative to LSODE. The error tolerances for the LSODE simulation were set such that the results for all species other than $O(^1D)$, H, and N should be accurate to within 1%, and in most cases much more accurate. The differences in Figure 1 show that the Onera-SIS solver can be considered accurate to the few percent level (integrating across all species) after a simulated month.

The species that exhibit larger relative differences are those species, Cl_2, OClO, BrCl, NO_3, and some others, whose production terms are closely related to photochemical behaviors around the terminator. These differences were expected as trade-offs of assumptions made in solver design. The results of a series of box model runs with time steps as short as 15 s supported the contention that the observed differences arose from the time step length rather than other unidentified problems. Differences for these species in these runs decreased monotonically as the time step decreased.

Figure 1b is analogous to Figure 1a, but for the full GMI model. The comparison of the Onera-SIS solver to the SMVGEAR II solver, for January 15 output of the GMI model for 46°N and 70 hPa with common initial conditions on January 1, was constructed for the zonal means. The overall level of agreement in Figure 1b is quite similar to Figure 1a, although transport interactions with photochemistry could affect the results in Figure 1b. The larger differences are again for those species whose concentrations are most sensitive to changing abundances near the terminator, where the Onera-SIS solver's fixed time step is expected to affect the solution relative to the variable time step in SMVGEAR II.

The next step in the comparison is the analysis of how the errors accumulate over the longer time integration necessary, for example, for the assessment calculations. Figure 1c shows the species comparisons for a full year calculation with both Onera-SIS and SMVGEAR II. This comparison is constructed somewhat differently, in that relative differences are calculated for each space-time point in the output before the distribution is formed. This is a more stringent test than the comparison of zonal or diurnal averages, as in Figures 1a and 1b, because the

Table 5. FFSLT Advection Scheme With Single-Tracer Transport (No Chemistry) Timing Dependence on Horizontal Resolution

Resolution	Timing (C90 Minutes per Simulated Year)[a]
2° × 2.5° resolution at 900 s time step	343
4° × 5° resolution at 900 s time step	106
4° × 5° resolution at 1800 s time step	55

[a]All with 44 level data.

Table 6. FFSLT Algorithm Tracer Transport (No Chemistry) Dependence on Number of Species

Number of Species	Timing (C90 Minutes per Simulated Year)[a]
1	55
10	449
25	1110
50	2182

[a]Timings for 1800 s time step at 4° by 5° resolution with 44 vertical layers.

Table 7. GMI Model Stratospheric Chemistry Timing Studies (Using FFSLT Advection) Split by Major Operator and Showing Dependence on Chemistry Solution Technique[a]

		Chemistry Solution Technique	
		SIS	SMVGEAR II
Physics operator	chemistry	242	321
	photolysis	21	21
	PSC/SAD	9	9
	transport	36	36
Total		308	387

[a]All runs use the same chemical mechanism. Timings are given as Cray C90 hours per simulated year, using the 4° by 5° by 44 meteorological field.

Table 8. GMI Model Stratospheric Chemistry Timing Studies Using the FFSLT Advection, Showing Dependence on Chemistry Solution Technique on the Cray T3E-600 and SGI Origin 2000 Platforms[a]

		Cray T3E-600	SGI Origin 2000
Chemistry solution technique	SIS	116	103
	SMVGEAR II	334	163

[a]All runs use the same chemical mechanism and involve all the modules needed for aircraft assessment. Timings are given as CPU hours per simulated year using 31 processors and the 4° by 5° by 44 meteorological field.

contribution of differences is not made relative to the constituent concentration. That is, a large relative difference encountered at some point in the stratosphere where the species is very small is given the same weight as a relative difference at the species' maximum abundance. The region of comparison was restricted to the stratosphere, and very small concentrations (less than 10^{-4} molecules cm^{-3} or a mole fraction of 10^{-24}, as appropriate) were excluded. The distribution was also area-normalized, but not weighted for altitude or ambient pressure. The open section of the bar represents the mean of the distribution for each species, and the hatched bar represents the relative difference value that includes 90% of the points in space and time. For HCl these values are actually inverted, in that the ninetieth percentile is less than the mean value, indicating a long tail on the distribution. This did not occur for any other species.

The results of this comparison (Figure 1c) show that differences accumulate slowly, an indication that the abundances of the trace species are buffered, by the photochemical environment, against transport-driven divergence of the solution. The grouping of species by solver difference and the magnitudes of the differences are similar to the results of the shorter runs in Figures 1a and 1b. This lends additional support to the choice of Onera-SIS for the assessment runs.

Finally, consideration of the distribution and the pattern of differences for each individual species can reveal whether the behavior can be explained by the nature of the mechanism and the expected effects of solver assumptions, or appears to signal some error in the solver. Figure 2 shows the solver difference distribution for ozone, plotted against the cumulative concentration distribution.

Ozone concentration as number density spreads over nearly 2 orders of magnitude, and the mean absolute difference between solvers is always less than 0.5%. At the locations of the upper 95% of ozone concentrations, 90% of the solver differences are within 1%. At the locations of the upper 50% of ozone concentrations, 99% of the solver comparisons are within 1%. The far outliers in the difference distribution tend to occur in the south polar spring, where heterogeneous processes are activating inorganic chlorine.

The case of ozone shows that distributions of differences, summarized in Figure 1 above, are not themselves evenly distributed in time and space. Differences in species with fast photochemical time constants tend to cluster around the terminator. The chemical relationship of species will cause differences in one species, for example, HO_2, to propagate to another, H_2O_2 in this case.

For most of the species with the largest average differences, solver differences for locations with concentrations in the upper decade (representing a few percent of the distribution) are

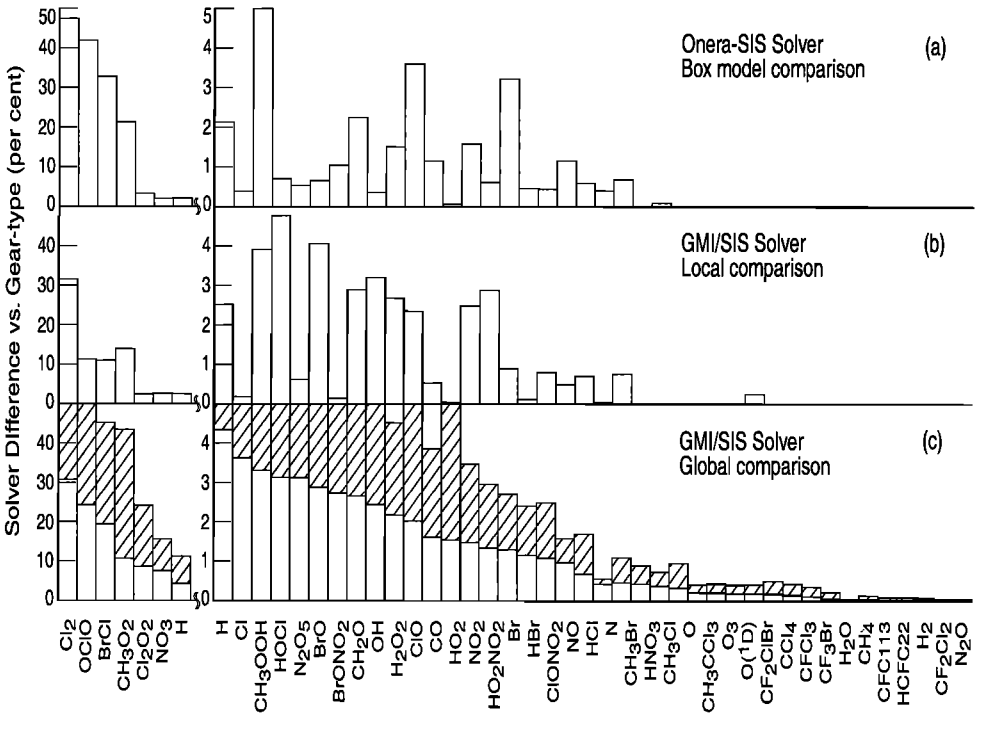

Figure 1. (a) Absolute value of the relative difference of the diel averages of the Onera-SIS solver relative to the LSODE solver for 48°N, 20 km, January 15, thirtieth day of repeating diel box model integration; (b) comparison of January 15 zonal mean at 46°N, 70 hPa for Onera-SIS in the GMI model to SMVGEAR II in the GMI model; (c) global, annual comparison of Onera-SIS to SMVGEAR II (see text for details).

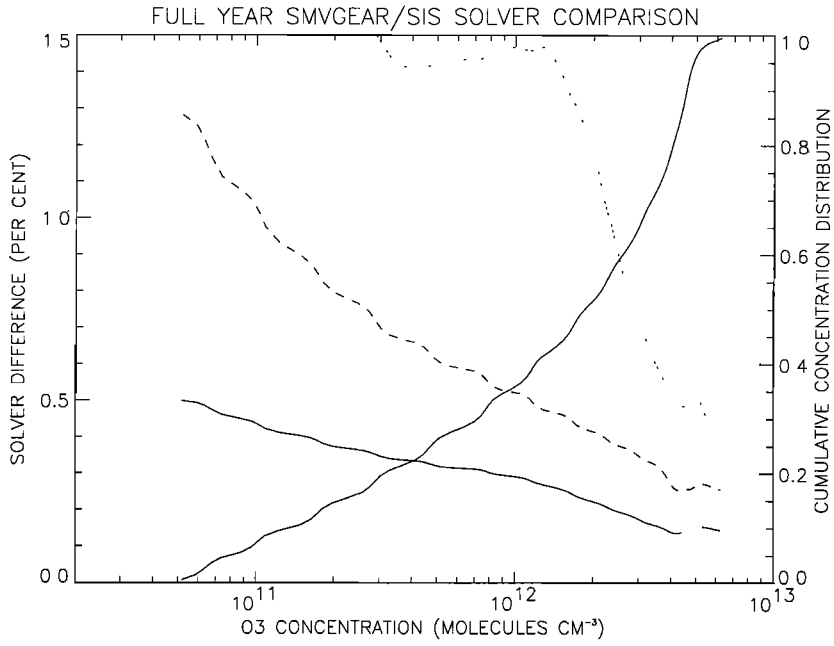

Figure 2. The cumulative probability distribution for ozone concentration in the GMI model is shown in the upward trending solid line and is associated with the right axis. The downward trending solid line is the mean of the absolute values of the solver differences for all points with ozone concentrations larger than the indicated concentration, that is, the fiftieth percentile of the difference distribution for concentrations at or above the threshold value. The dashed line is the ninetieth percentile difference value, for which 90% of the differences are smaller than the plotted value for all points with equal or greater ozone concentrations. The dotted line is the 99th percentile.

much smaller than the mean. For example, Cl_2 differences for the upper decade of concentration average about 8%, with differences of about 2% for the largest concentrations. Regions of heterogeneous activation of inorganic chlorine are also characterized by larger differences. For CH_3O_2, solver differences actually increase with number density in the cumulative distribution, as the largest concentrations are reached when atomic Cl is large, in the austral polar spring, as a result of the Cl + CH_4 reaction, which is usually of lesser importance.

It is, perhaps, important to note that the solver differences shown in the figures above are, in almost every case, not visible comparing the solvers side by side on the conventional contour or false color plot. The decision to select Onera-SIS for the GMI assessment calculations was made qualitatively on a cost-benefit basis, trading computational performance against accuracy of the photochemical species abundances, in the light of the necessity to complete a set of assessment runs.

7. Transport Model Application and Validation

As discussed earlier, the GMI model incorporated the flux form semi-Lagrangian scheme as its primary transport operator. We have validated the meteorological data and transport model implementation through simulations of stratospheric tracers and comparisons to similar model runs at the originating organization. Three test cases provided the primary comparison: a steady state N_2O simulation, the NASA Models and Measurements II [*Park et al.*, 1999] Age of the Air diagnostic (MMII A1), and the NASA Models and Measurements II Artificial NO_x type tracer (MMII A3).

This validation took place in two stages. After implementing the transport algorithms and meteorological data into the GMI model, the first stage used N_2O simulations to test the implementation of the advection operator and the meteorological data. Using tabulated values of monthly averaged loss rates (from photolysis and O^1D loss (M. Prather, personal communication, 1995)), we tested these models against simulations of N_2O made using the parent models from which the GMI advection schemes were taken. In each case, we were able to match the simulations very well indicating that the advection schemes and meteorological data sets were correctly implemented. The second, and more interesting stage, was to evaluate the application of the FFSLT algorithm to the three meteorological data sets. For this evaluation, in addition to N_2O, we also used the NASA Models and Measurements II A1 and A3 tracers. The A1 tracer was a diagnostic to generate the age spectrum of the atmospheric model. The A3 tracer was the emissions of a hypothetical tracer from a projected fleet of high-speed civil transports (HSCTs). For more information on the NASA MMII tracer and analysis, see *Park et al.* [1999]. The goal was to compare the long-lived tracer distributions obtained using FFSLT to those distributions obtained using the parent model's advection scheme. Thus, in stage one, we ran the NCAR meteorological data through the NCAR SLT routine and reproduced the correct profiles. Next we used the NCAR meteorological data through the FFSLT advection routine to investigate differences in the profiles caused by the different advection operator.

Figure 3a shows the N_2O zonal averaged (steady state) profiles from the MACCM2 meteorological data and the NCAR SLT algorithm. Figure 3b shows the same calculation using the FFSLT advection operator. Comparing Figures 3a and 3b shows the profiles of N_2O to be very faithfully reproduced using the FFSLT advection operator. In its current form the FFSLT routine requires grids with equally spaced grids in the

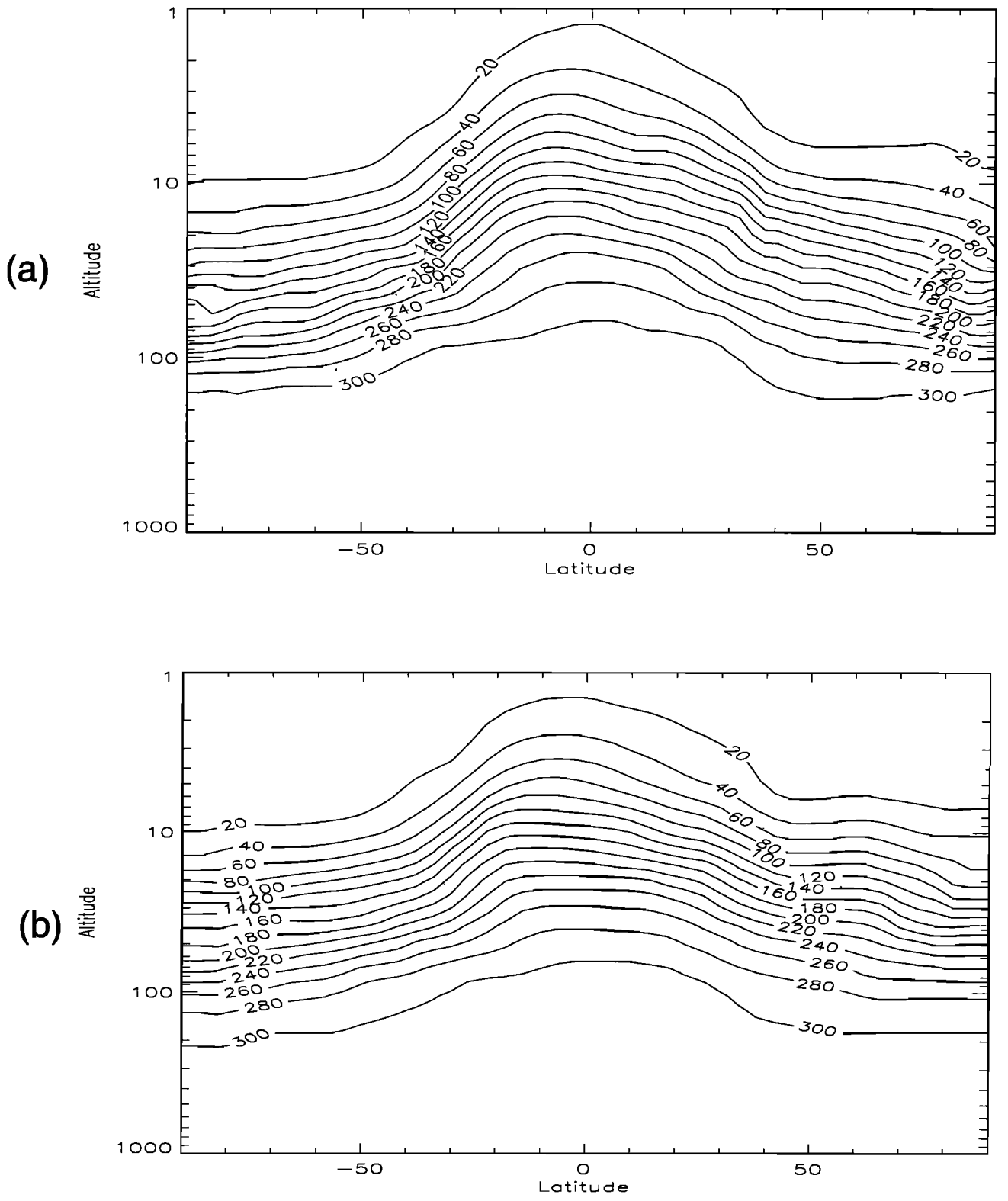

Figure 3. Steady state zonal averaged N_2O simulation results for January using the GMI model. (a) Results obtained using the NCAR MACCM2 meteorological input data with the semi-Lagrangian advection algorithm. (b) Results obtained using the NCAR MACCM2 meteorological input data with the flux form semi-Lagrangian advection scheme. Units are ppbv.

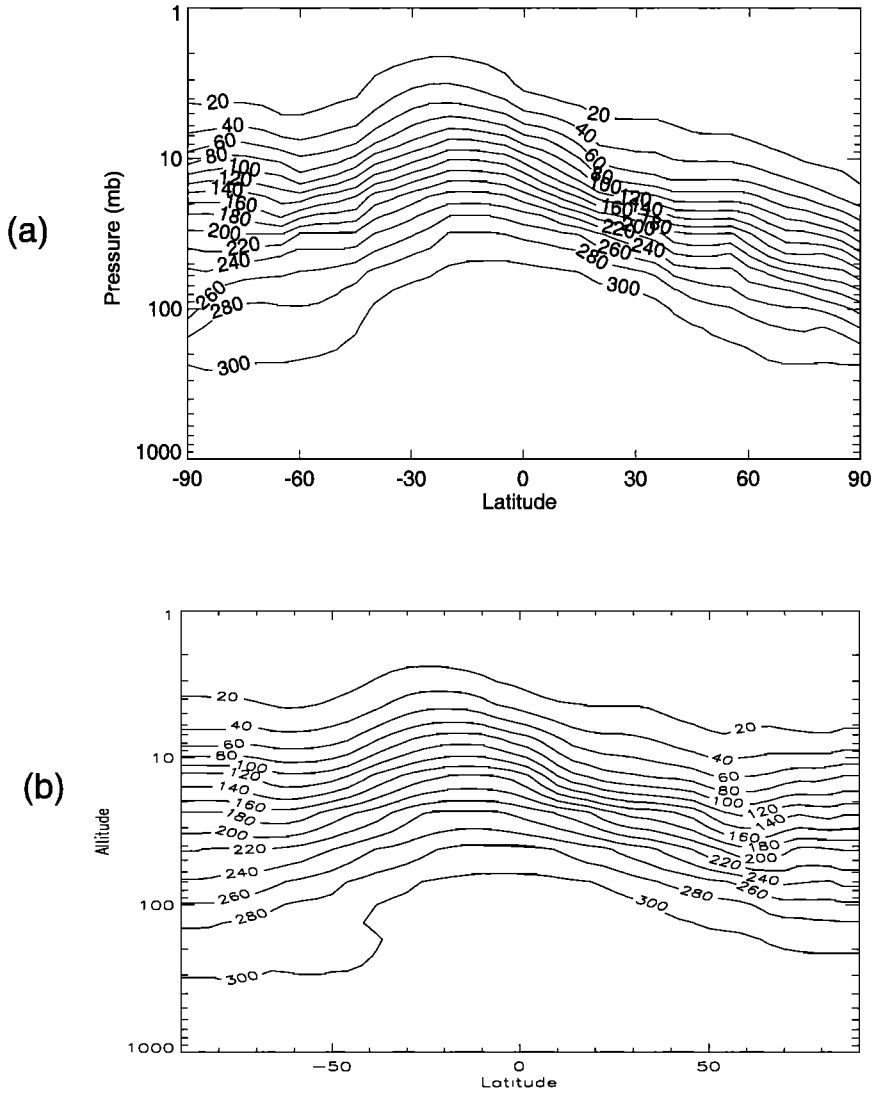

Figure 4. Steady state zonal averaged N_2O simulation results for January using the GMI model. (a) Results obtained using the GISS II′ meteorological input data with the second-order moment method advection scheme. (b) Results obtained using the GISS II′ meteorological input data with the flux form semi-Lagrangian advection scheme. Units are ppbv.

latitude and longitude direction. Since the MACCM3 data were originally provided on a Gaussian grid, the data were interpolated onto a fixed 4° by 5° grid. Even with this additional interpolation, the results match very well. The NCAR SLT routine appears to be slightly better in keeping a stronger gradient in the extratropical regions, but it is not clear whether this is an advection scheme issue or an issue arising from the added interpolation.

Figure 4a shows the N_2O zonal averaged (steady state) profile from the GISS II meteorological data and the UCI second-order moment (SOM) advection scheme. Figure 4b shows the profile from the GISS II data obtained using the FFSLT scheme. Comparisons of these plots show the SOM is better able to maintain gradients in the N_2O profiles, but the overall structure is reproduced very well.

It should be noted that in both of these cases, the FFSLT scheme is calculating the vertical fluxes from the input horizontal wind data. We have assessed the predicted vertical mass fluxes in the FFSLT and in the other advection routines, and in both cases, the FFSLT has accurately calculated the same vertical fluxes that the SLT and SOM predict when using those meteorological data. This validation and sensitivity test suggests that for long-lived tracers, like N_2O, the particular characteristics of the advection operator do not influence the distribution. This does not address whether the N_2O simulations reproduce observed data. That has been addressed by *Douglass et al.* [1999].

Another test of the sensitivity of stratospheric transport to advection operator is the age diagnostic as defined by the NASA Models and Measurements II workshop (see *Park et al.* [1999] for details). In short, this test case inputs a short (month long) pulse of tracer into the equatorial lower troposphere, then stops the pulse and imposes a loss rate in the troposphere. The speed at which the tracer is eliminated from the troposphere by dynamics of the stratosphere through stratosphere/troposphere exchange is representative of the residence time and overturning rate of the stratosphere. Figures 5a and 5b show the mean age of the MACCM2 meteorological data as

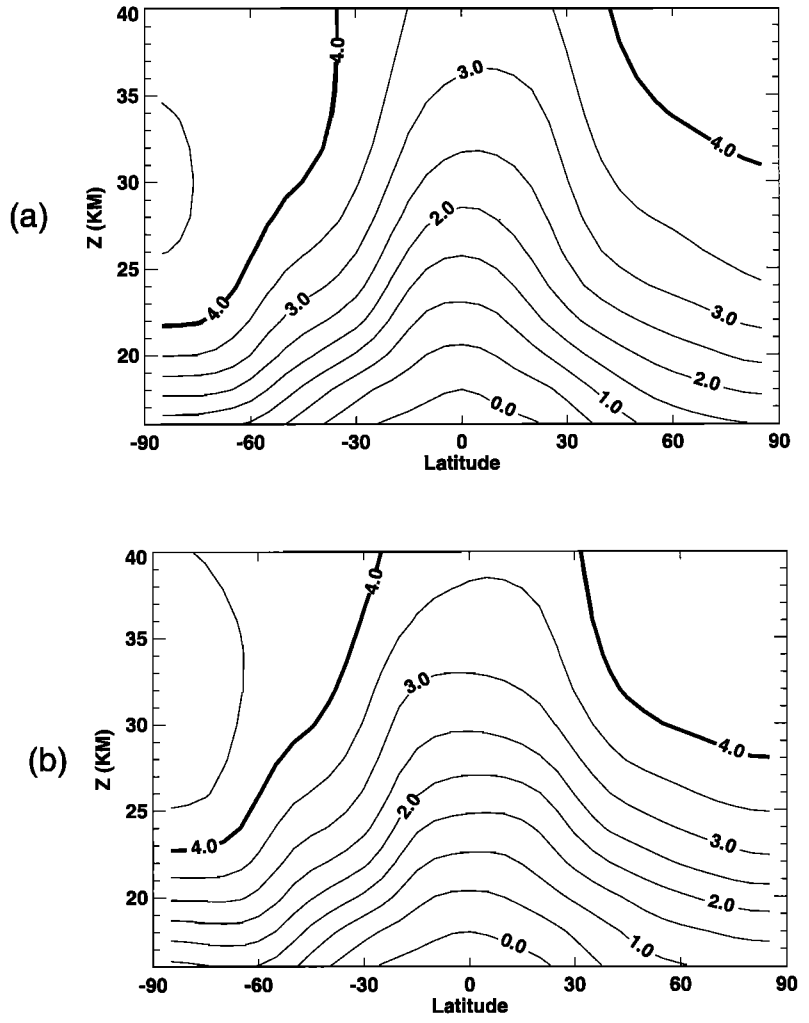

Figure 5. Mean age of air as calculated with the NCAR MACCM2 meteorological input data with (a) the semi-Lagrangian advection scheme and (b) the flux form semi-Lagrangian scheme. Units are years.

simulated using the SLT and FFSLT (respectively) and Figures 6a and 6b show the same using the GISS data. Again, the GMI model results match the original model results very well. It should be noted that observations suggest stratospheric air with a mean age that is longer than simulated with either MACCM2 or GISS II [see *Hall et al.*, 1999]. As noted in the NASA MMII report [*Park et al.*, 1999] and by *Hall et al.* [1999], this is characteristic of most two- and three-dimensional atmospheric models and is still an area of intense research.

The GMI model was developed to produce assessments of the environmental consequences from the emissions of a proposed fleet of supersonic aircraft. The NASA Models and Measurements II constructed a test problem, the A3 tracer test, to evaluate the ability of a model to simulate a tracer representing aircraft emissions. The A3 tracer run was based on an HSCT emission scenario [*Baughcum and Henderson*, 1998] assuming 500 HSCTs flying between 17 and 20 km with a NO_x emission index of 10 grams (as NO_2)/kilogram of fuel burned [*Park et al.*, 1999]. The tracer was emitted via these scenarios and lost via elimination if the tracer moved to within 6 km of the surface. Simulations are run until steady state. Figure 7 shows the results of the GMI model with all three meteorological data sets and those produced by the parent organization of the data sets. All distributions in the first column were obtained using the GMI model with the FFSLT advection scheme, hence differences show the sensitivity to the meteorological data. The top row represents the simulations of the GMI and GSFC using the DAO assimilation data. In this case, the GSFC simulation used the same advection operator but was run at a higher resolution (2° by 2.5° versus 4° by 5° in the GMI simulation). This higher resolution better maintains the tracer in the region of emission and, in particular, allows less transport of tracer into the Southern Hemisphere. The middle panel shows the simulation using the MACCM2 meteorological fields in the GMI model and the NCAR MATCH model using the NCAR SLT advection scheme. These simulations show large differences. Through additional testing and analysis, it is believed this difference is caused by the "mass fixer" required within the SLT algorithm in the MATCH model. Further testing (D. Waugh, private communication, 1998) showed that distributions of this tracer differed greatly when the mass fixer was or was not used. Recall that in Figure 1 we showed that for N_2O there were no significant differences between simulations carried out with the FFLST and SLT advection schemes. However, for the HSCT tracer (Figure 7) this same advection scheme comparison shows large differences. Possibly, the influence of the mass fixer is greater for those species whose maximum concentrations occur in the

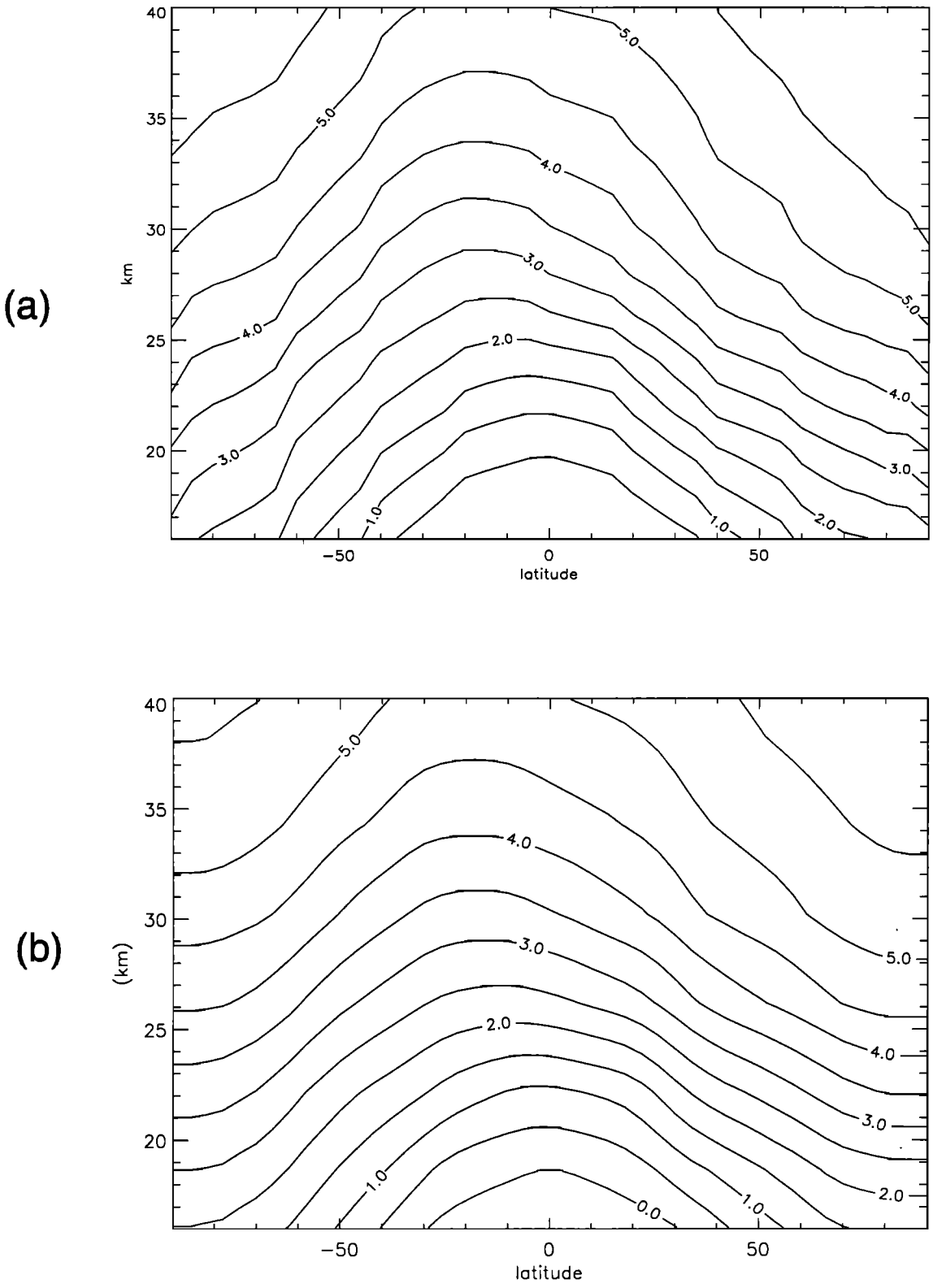

Figure 6. Mean age of air as calculated with the GISS II′ meteorological input data with (a) the second-order moment advection scheme and (b) the flux form semi-Lagrangian scheme. Units are years.

stratosphere (like the HSCT) versus those whose maximum is near the surface (like N_2O). The bottom panel shows the A3 simulation using the GISS II data in both the GMI model and the UCI CTM using the SOM advection scheme. The simulations compare very well. We conclude from these simulations that the SLT scheme is not well suited to studies of stratospheric aircraft emissions since simulation results are strongly dependent on the use (or nonuse) of the mass fixer.

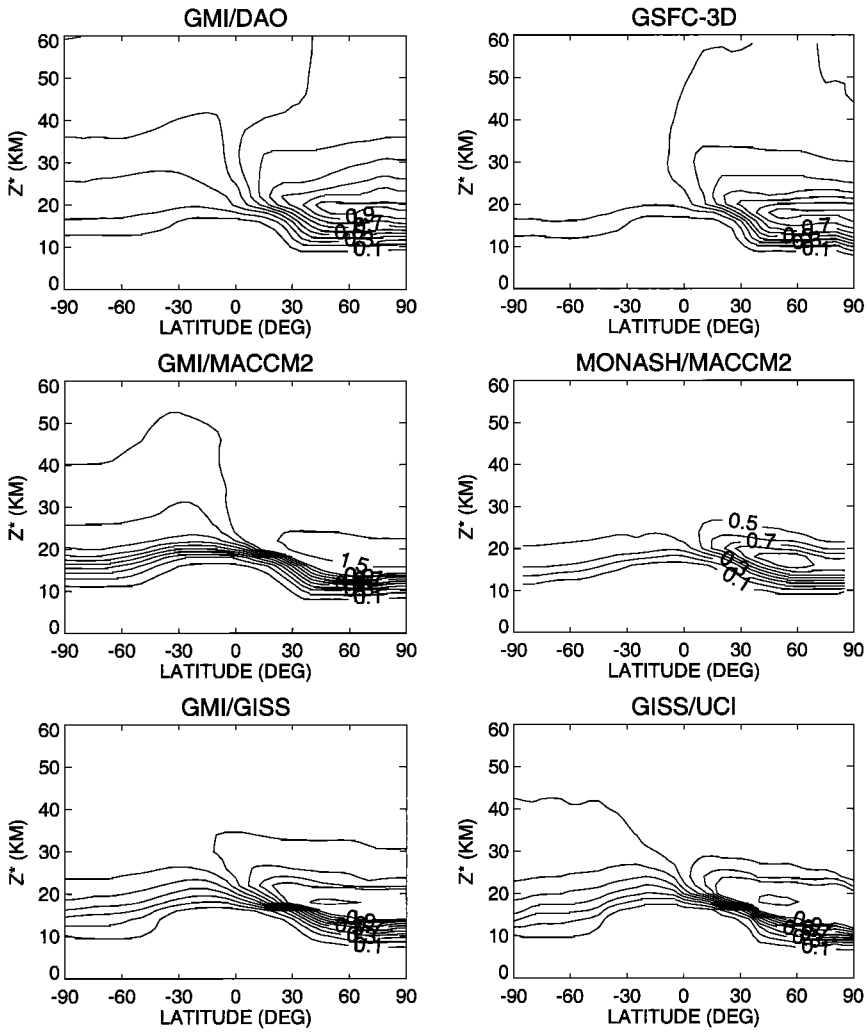

Figure 7. Steady state simulations of NO_x-like aircraft emissions (NASA MMII tracer A3). (top) Results from a 4° by 5° horizontal resolution simulation (GMI/DAO) and a 2° by 2.5° horizontal resolution (GSFC-3-D) using the NASA DAO assimilation input data. Simulations show higher horizontal resolution to isolate tracer to emission region. (middle) Results from MACCM2 input data in the flux form semi-Lagrangian transport algorithm and the semi-Lagrangian algorithm. Differences were attributable to the use of a mass fixer in the semi-Lagrangian algorithm. (bottom) Good agreement between the flux form semi-Lagrangian and second-order moment advection schemes. Units are ppbv.

Distributions in the first column of Figure 7 show only the influence of input meteorological data on the HSCT emission distribution (all other aspects of the model were held constant). Studies carried out in MMII showed the mean age in the DAO meteorological data to be less than those of the MACCM2 and GISS II′ [see *Park et al.*, 1999]. Distributions in Figure 7 suggest that for those models with lower mean ages (DAO), they accumulate less exhaust material in the lower stratosphere. Recent work by *Hall and Waugh* [2000] suggests there may be a more quantitative relationship, albeit not perfect, between mean age and buildup of aircraft emissions. For example, they suggest that a mean age of 3 years suggests a typical residence time of aircraft emissions of 1.1 to 2.1 years, while reducing the mean age to 2 years reduces the residence time to 0.6 to 1.2 years. For more discussion of this subject, see *Kawa et al.* [1999].

8. Sensitivity of Simulations to Advection Scheme Parameters

The GMI model's primary advection algorithm is the flux form semi-Lagrangian transport (FFSLT) [*Lin and Rood*, 1996]. Within its algorithmic structure there are multiple choices for monotonicity constraints that have implications on the subgrid tracer distribution used to calculate fluxes across cell edges. In an effort to understand the sensitivities of tracer simulations to the selection of these constraints, we have carried out further simulations of MM II A1 and A3 using the FFSLT scheme. In the nomenclature of the FFSLT scheme these various choices are referred to as ORDs, and one has choices of these constraints in the horizontal and vertical directions (i.e., IORD, JORD, and KORD). In our simulations the sensitivities seem to be small with respect to IORD and

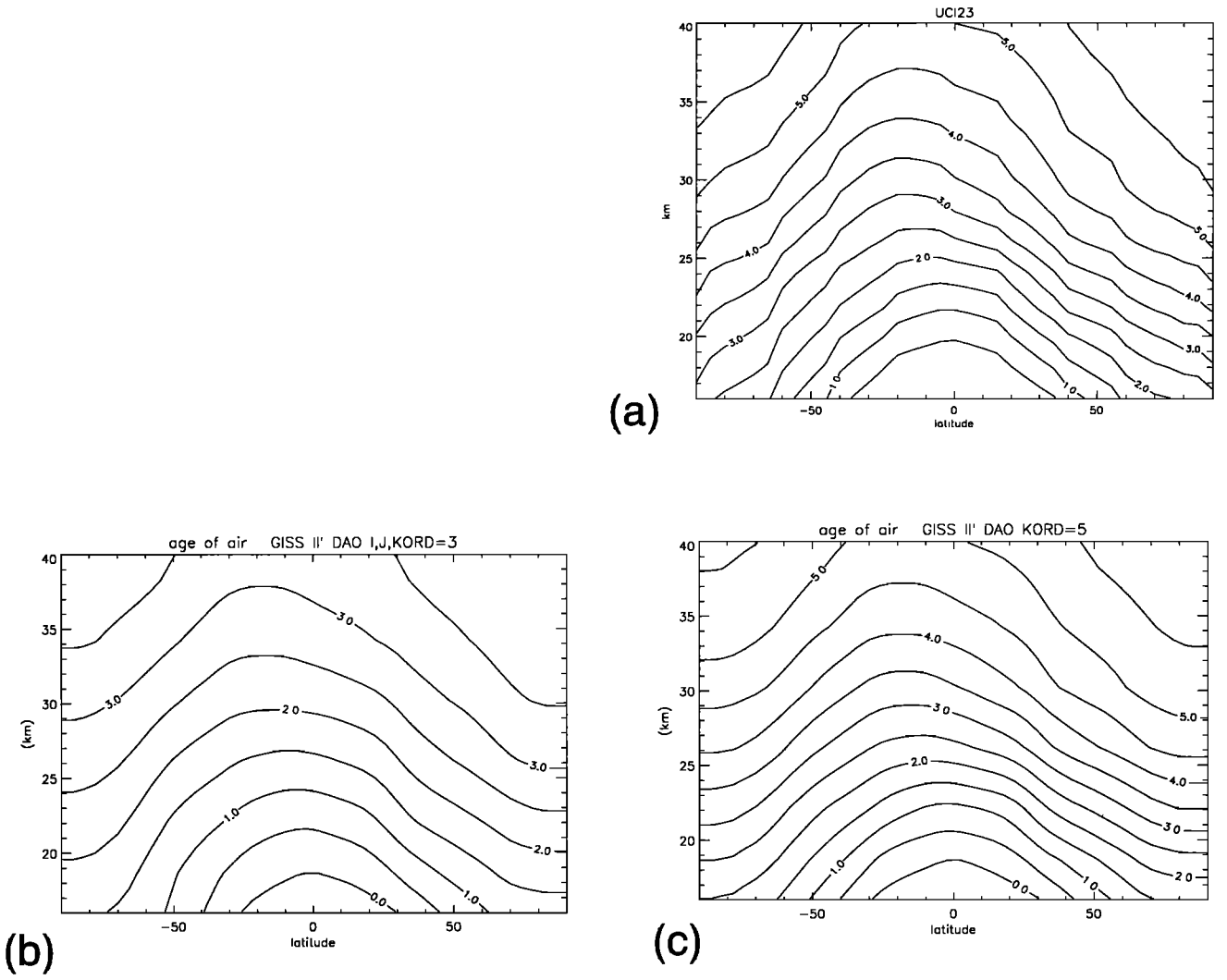

Figure 8. NASA MMII A-1 age diagnostic using the GISS II′ input meteorological data. Figure shows the second-order method scheme results and those of two versions of the flux form semi-Lagrangian (FFSLT) method. Case A of the FFSLT used a monotonicity constraint that allowed no overshoots and undershoots. Case B of the FFSLT used a monotonicity constraint that allowed only overshoots (remained positive definite). Results show the simulations to be highly dependent on this constraint. Analysis showed the dependence to be attributable to the constraint and the coarse vertical resolution of the GISS II′ data in the region of the tropopause. Units are years.

JORD; however, important differences appear when altering the KORD. We will show these differences using the MMII A1 and A3 tracer using FFLST and the GISS II winds. Similar differences occur when using the DAO and NCAR data sets, but the differences are smaller (we will use this fact to better understand our results).

Figure 8 shows the MMII A1 tracer run SOM and FFSLT with the GISS II data set. Figure 8a shows output using the UCI-SOM advection scheme. Figure 8b represents FFSLT simulations using KORD = 3, while those in Figure 8c represents those from a run using KORD = 5. The KORD = 5 results match the original UCI-produced age very well (and was used in Figure 6). However, when using KORD = 3, the age of the stratosphere is much younger; by nearly 2 years. Recall, these KORD values represent different choices of monotonicity constraints and, in general, one can associate reduced diffusion with increasing values of KORD (for details on the exact definitions of the KORD parameters, see *Lin and Rood* [1996, Appendix A.3]. Figure 9 shows simulations of the MM II A3 tracer which also show large differences in the buildup of tracer emissions in the lower stratosphere when using KORD = 3 (Figure 9a) and KORD = 5 (Figure 9b). Further investigations showed these differences to be related to vertical resolution. While these comparison simulations were done with all the meteorological data sets, the GISS II set produced the most marked differences. The GISS II set also has the coarsest vertical resolution in the tropopause region, identical to the region of tracer input. This is likely one of the causes that leads to the larger differences in the GISS II′. Differences when using KORD = 5 or KORD = 3 appear to be problem-dependent. Figure 4 showed N_2O distributions using FFSLT and GISS II′ winds. In this case, the solution was smoother through the tropopause region, and the results did not depend on the choice of KORD.

By design, the GMI model allows these types of comparison simulations to be carried out and greatly aids in the under-

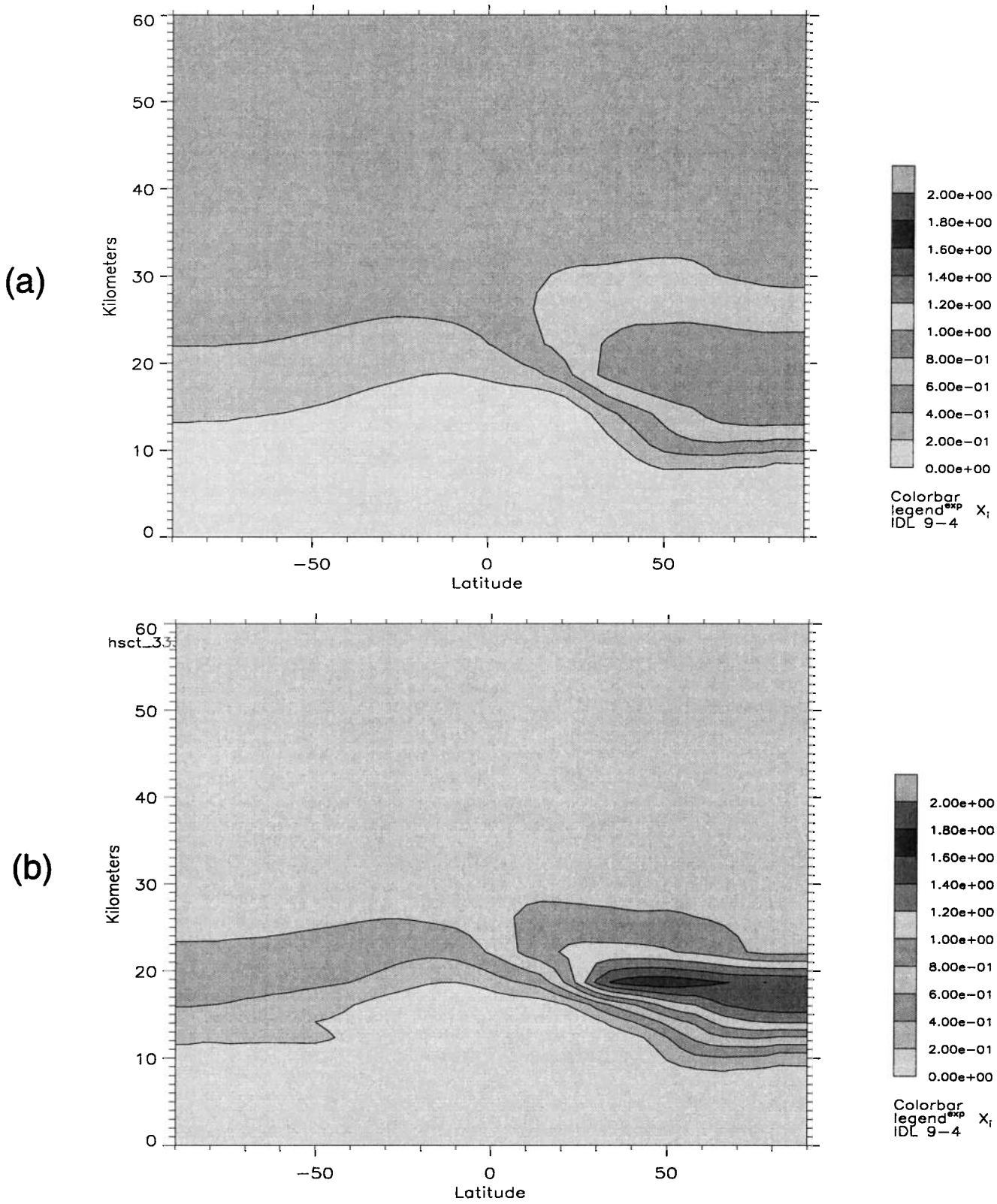

Figure 9. Steady state NO_x-like tracer using the flux form semi-Lagrangian transport algorithm and the GISS II′ meteorological data. Simulation results show a large difference in buildup of aircraft emissions depending on the advection algorithm characteristics: (a) with monotonicity constraint allowing no overshoots and undershoots and (b) allowing only overshoots (remains positive definite). Analysis showed this dependence to be attributable to the constraint and the coarse vertical resolution of the GISS II′ data in the region of the tropopause. Units are ppbv.

standing of model simulations. This analysis can also be extended to other results. For example, the MMII report [*Park et al.*, 1999] shows large variations in simulation results from the MM II A3 tracer (and others). Given the variations seen by simply changing the monotonicity constraint in the advection scheme in the GMI model, one could argue that different advection schemes, different meteorological data, and different model structures throughout the entire MM II model suite should easily be able to produce the variety of results seen in the simulation output. Such variations also point to the need for GMI-type frameworks where science modules can be interchanged and intercompared. Moreover, this capability coupled with comparisons to observations (such as *Douglass et al.* [1999] and J. M. Rodriguez et al. (manuscript in preparation, 2000)) provide an important pathway toward improved understanding of assessment simulations.

9. Conclusions

The NASA High Speed Research Program was tasked with providing an assessment of the possible environmental consequences caused by the emissions of a proposed fleet of supersonic aircraft. Past aircraft assessments made use of two-dimensional chemical transport models to provide impacts of the emissions on stratospheric ozone. Measurements and simulations have both pointed toward the need for three-dimensional models to accurately assess the response of lower stratospheric ozone. The NASA Global Modeling Initiative and its science team was created to provide a robust, well tested and evaluated, and computationally advanced three-dimensional chemical transport model to provide assessment simulations and analysis. This model and framework is referred to as the GMI core model. We have described a modeling structure designed to allow controlled numerical experimentation to better understand model simulations toward enabling a more robust and well understood assessment simulation. The model structure allows intercomparison and diagnosis of individual physics and numerical modules and allows an understanding of sensitivities of simulation results to the numerical algorithms and chemical/physical approaches taken. Extensive comparisons to observations are given by *Douglass et al.* [1999] and J. M. Rodriguez et al. (manuscript in preparation, 2000). The model runs on a variety of platforms including massively parallel computers. We have used this model to produce assessment simulations of a proposed fleet of supersonic aircraft [*Kawa et al.*, 1999; *Kinnison et al.*, this issue].

The framework includes three different meteorological inputs (NASA DAO, NCAR MACC2, and the GISS II′), three different advection schemes (flux form semi-Lagrangian, semi-Lagrangian, and the second-order moment method), two different numerical algorithms for chemistry solutions (SMVGEAR II and the semi-implicit method), along with algorithms to provide mass consistent meteorological data, heterogeneous chemical processes on type 1 and type 2 polar stratospheric clouds, and diagnostics for model simulation analysis. Simplified parameterizations for tropospheric physics are included to wet deposit chemical species. The chemical mechanism is focused on stratospheric chemistry with simplified chemistry in the troposphere (i.e., methane). The mechanism includes photolytic and thermal reactions of species in the species families of O_x, NO_y, ClO_y, HO_y, BrO_y, CH_4, and its oxidation products. Photolysis rates are provided by a lookup table.

To evaluate the model performance in the transport of chemical species, we have applied the GMI core model to the NASA Model and Measurement II tracer tests: MMII A1 (age diagnostic) and MMII A3 (aircraft-emitted NO_x-like tracer) as well as N_2O. The model was tested to ensure accurate implementation of the numerical algorithms and was also applied to understand the sensitivity of meteorological input data and numerical algorithms to simulated tracer transport. Studies discussed in this paper show the models to faithfully reproduce simulation results from the data/algorithm parent organization. The ability of the model to swap numerical algorithms and input data enabled the model to examine the sensitivity of algorithms and input data on simulation results. Results show the N_2O tracer to be relatively independent of numerical algorithm; however, the tracers of the age diagnostic and the aircraft NO_x-like tracer are shown to be very dependent on the numerical algorithm used in the advection operator.

Future work with the GMI model will extend its application to more meteorological data sets and more detailed tropospheric chemistry and transport, where, for example, the model can be used to study the influence of convective transport formulation on species distributions. A particular application will be studying the perturbation caused by the emissions from current and projected fleets of subsonic (commercial) aircraft and analyzing the impacts on ozone and ozone chemistry with possible feedbacks to clouds and climate.

Acknowledgments. The authors would like to thank the entire GMI Science Team for their collaborative effort toward this model. We would also like to thank Steve Baughcum for his many comments on this document. This work was performed under the auspices of the U.S. Department of Energy by the Lawrence Livermore National Laboratory under contract W-7405-ENG-48. Lawrence Livermore authors were supported by NASA contract S-10161-X.

References

Albritton, D. L., et al., The Atmospheric Effects of Stratospheric Aircraft: Interim assessment report of the NASA High-Speed Research Program, *NASA Ref. Publ.*, *1333*, 1993.

Anderson, D. E., R. DeMajistre, S. Lloyd, and P. Swaminathan, Impact of aerosols and clouds on the troposphere and stratosphere radiation field with application to twilight photochemistry at 20 km, *J. Geophys. Res.*, *100*, 7135–7145, 1995.

Andrews, D. G., and M. E. McIntyre, Planetary waves in horizontal and vertical shear: The generalized Eliassen-Palm relation and the zonal mean acceleration, *J. Atmos. Sci.*, *33*, 2031–2048, 1976.

Baughcum, S. L., and S. C. Henderson, Aircraft emission scenarios projects in year 2015 for the NASA Technology Concept Aircraft (TCA) High Speed Civil Transport, *NASA Contract. Rep.*, *CR-1998-207635*, 1998.

Boville, B. A., J. R. Holton, and P. W. Mote, Simulations of the Pinatubo aerosol cloud in general circulation model, *Geophys. Res. Lett.*, *18*, 2281–2284, 1991.

Brown, S. S., R. K. Talukdar, and A. R. Ravishankara, Rate constants for the reaction $OH + NO_2 + M \rightarrow HNO_3 + M$ under atmospheric conditions, *Chem. Phys. Lett.*, *299*, 277–284, 1999.

Carslaw, K. S., B. Luo, and T. Peter, An analytic expression for the composition of aqueous HNO_3-H_2SO_4 stratospheric aerosols including gas phase removal of HNO_3, *Geophys. Res. Lett.*, *22*, 1877–1880, 1995.

Chipperfield, M. P., D. Cariolle, P. Simon, R. Ramaroson, and D. J. Lary, A three-dimensional modeling study of trace species in the arctic lower stratosphere during winter 1989–1990, *J. Geophys. Res.*, *98*, 7199–7218, 1993.

Claveau, J., and R. Ramaroson, First simulation of the transport and the chemical transformation of chemical species with a mesoscale-regional model: MEDIUM, paper presented at International Col-

loquium on Effects of Aircraft Upon the Atmosphere, Off. Natl. d'Etud. et Rech. Aerosp., Paris, France, Oct. 15–18, 1996.

Considine, D. B., A. R. Douglass, P. S. Connell, D. E. Kinnison, and D. A. Rotman, A polar stratospheric cloud parameterization for the three-dimensional model of the global modeling initiative and its response to stratospheric aircraft emissions, *J. Geophys. Res.*, *105*, 3955–3975, 2000.

DeMore, W. B., S. P. Sander, D. M. Golden, R. F. Hampson, M. J. Kurylo, C. J. Howard, A. R. Ravishankara, C. E. Kolb, and M. J. Molina, Chemical kinetics and photochemical data for use in stratospheric modeling, Evaluation 12, *JPL Publ.*, *97-4*, 1997.

Douglass, A. R., M. A. Carroll, W. B. DeMore, J. R. Holton, I. S. A. Isaksen, and H. S. Johnston, The Atmospheric Effects of Stratospheric Aircraft: A current consensus, *NASA Ref. Publ.*, *1251*, 1991.

Douglass, A. R., R. B. Rood, C. J. Weaver, M. C. Cerniglia, and K. F. Brueske, Implications of three-dimensional tracer studies for two-dimensional assessments of the impact of supersonic aircraft on stratospheric ozone, *J. Geophys. Res.*, *98*, 8749–8963, 1993.

Douglass, A. R., R. Rood, S. Kawa, and D. Allen, A three-dimensional simulation of the evolution of the middle-latitude winter ozone in the middle stratosphere, *J. Geophys. Res.*, *102*, 19,217–19,232, 1997.

Douglass, A. R., M. P. Prather, T. M. Hall, S. E. Strahan, P. J. Rasch, L. C. Sparling, L. Coy, and J. M. Rodriguez, Choosing meteorological input for the global modeling initiative assessment of high-speed aircraft, *J. Geophys. Res.*, *104*, 27,545–27,564, 1999.

Dunkerton, T., On the mean meridional mass motions of the stratosphere and mesosphere, *J. Atmos. Sci.*, *35*, 2325–2333, 1978.

Gear, W., The numerical integration of ordinary differential equations, *Math. Comput.*, *21*, 146–156, 1967.

Gierczak, T., J. B. Burkholder, and A. R. Ravishankara, Temperature dependent rate coefficient for the reaction $O(^3P) + NO_2 \rightarrow NO + O_2$, *J. Phys. Chem. A*, *103*, 877–883, 1999.

Goldfarb, L., M. H. Harwood, J. B. Burkholder, and A. R. Ravishankara, Reaction of $O(^3P)$ with $ClONO_2$: Rate coefficients and yield of NO_3 product, *J. Phys. Chem. A*, *102*, 8556–8563, 1998.

Graedel, T. E., Statement before the Subcommittee on Technology, Environment, and Aviation, Committee on Science, Space, and Technology, U.S. House of Representatives, Washington, D. C., 1994.

Hall, T. M., and D. Waugh, Stratospheric residence time and its relationship to mean age, *J. Geophys. Res.*, *105*, 6773–6782, 2000.

Hall, T. M., D. Waugh, K. Boering, and A. Plumb, Evaluation of transport in stratospheric models, *J. Geophys. Res.*, *104*, 18,815–18,839, 1999.

Hanson, D., and K. Mauersberger, Laboratory studies of the nitric acid trihydrate: Implications for the south polar stratosphere, *Geophys. Res. Lett.*, *15*, 855–858, 1988.

Hartley, D. E., D. Williamson, P. Rasch, and R. Prinn, Examination of tracer transport in the NCAR CCM2 by comparison of CFCl3 simulations with ALE/GAGE observations, *J. Geophys. Res.*, *99*, 12,855–12,896, 1994.

Hofmann, D. J., and S. Solomon, Ozone destruction through heterogeneous chemistry following the eruption of El Chichon, *J. Geophys. Res.*, *94*, 5029–5041, 1989.

Intergovernmental Panel on Climate Change (IPCC), *Special Report on Aviation and the Global Atmosphere*, edited by J. E. Penner et al., Cambridge Univ. Press, New York, 1999.

Jacobson, M. Z., Computation of global photochemistry with SMVGEAR II, *Atmos. Environ.*, *Part A*, *29*, 2541–2546, 1995.

Kasten, F., Falling speed of aerosol particles, *J. Appl. Meteorol.*, *7*, 944–947, 1968.

Kawa, S. R., et al., Assessment of the effects of high-speed aircraft in the stratosphere: 1998, *NASA Tech. Pap.*, *TP-1999-209237*, 1999.

Kinnison, D. E., et al., Global Modeling Initiative assessment model: Application to high-speed civil transport perturbation, *J. Geophys. Res.*, this issue.

Lambert, J. D., *Computational Methods in Ordinary Differential Equations*, John Wiley, New York, 1974.

Lin, S.-J., and R. B. Rood, Multi-dimensional Flux-Form Semi-Lagrangian transport schemes, *Mon. Weather Rev.*, *124*(9), 2046–2070, 1996.

Lipson, J. B., M. J. Elrod, T. W. Beiderhase, L. T. Molina, and M. J. Molina, Temperature dependence of the rate constant and branching ratio for the OH + ClO reaction, *J. Chem. Soc. Faraday Trans.*, *93*, 2665–2673, 1997.

Logan, J. A., Nitrogen oxides in the troposphere: Global and regional budgets, *J. Geophys. Res.*, *88*, 10,785–10,807, 1983.

Marti, J., and K. Mauersberger, A survey and new measurements of ice vapor pressure at temperatures between 170 and 250 K, *Geophys. Res. Lett.*, *20*, 363–366, 1993.

Mirin, A. A., et al., Climate system modeling using a domain and task decomposition message-passing approach, *Comput. Phys. Commun.*, *84*, 278–296, 1994.

Oort, A. H., Global atmospheric circulation statistics, 1958–1983, *NOAA Prof. Pap.*, *14*, 1983.

Park, J., M. K. W. Ko, R. A. Plumb, and C. Jackman (Eds.), Report of the 1998 Models and Measurements Workshop II, *NASA Tech. Memo.*, *TM-1999-209554*, 1999.

Peter, T., C. Bruhl, and P. Crutzen, Increase in the PSC-formation probability caused by high-flying aircraft, *Geophys. Res. Lett.*, *18*, 1465–1468, 1991.

Prather, M. J., Numerical advection by conservation of second-order moments, *J. Geophys. Res.*, *91*, 6671–6681, 1986.

Prather, M. J., and E. E. Remsberg (Eds.), The Atmospheric Effects of Stratospheric Aircraft: Report of the 1992 Models and Measurements Workshop, *NASA Ref. Publ.*, *1292*, 1993.

Prather, M., M. McElroy, S. Wofsy, G. Russell, and D. Rind, Chemistry of the global troposphere: Fluorocarbons as tracers of air motion, *J. Geophys. Res.*, *92*, 6579–6613, 1987.

Prather, M. J., H. L. Wesoky, R. C. Miake-Lye, A. R. Douglass, R. P. Turco, D. J. Wuebbles, M. K. W. Ko, and A. L. Schmeltekopf, The Atmospheric Effects of Stratospheric Aircraft: A first program report, *NASA Ref. Publ.*, *1272*, 1992.

Ramaroson, R., Local, one and three dimensional modeling of chemical processes in the middle atmosphere, Ph.D. thesis, Univ. Paris VI, Paris, France, 1989.

Ramaroson, R., D. Cariolle, and M. Pirre, Simulation of Noxon Cliff in a three-dimensional model with diurnal variations during an unperturbed winter, in *Proceedings of the First European Workshop on Polar Stratospheric Ozone Research, Schlieersee FRG, 3–5 October 1990*, edited by J. Pyle, N. R. P. Harris, Cambridge, England, 1991.

Ramaroson, R., M. Pirre, and D. Cariolle, A box model for on-line computations of diurnal variations in multidimensional models: Application to the one-dimensional case, *Ann. Geophys.*, *10*, 416–428, 1992a.

Ramaroson, R., M. Pirre, and D. Cariolle, Qualitative study of the behavior of minor species during a stratospheric warming with a 3-D model, paper presented at Quadrennial Ozone Symposium, Int. Ozone Comm., Charlottesville, Va., June 1992b.

Rasch, P. J., and D. L. Williamson, Sensitivity of a general circulation climate model to the moisture transport formulation, *J. Geophys. Res.*, *96*, 13,123–13,137, 1991.

Rasch, P. J., X. Tie, B. A. Boville, and D. L. Williamson, A three-dimensional transport model for the middle atmosphere, *J. Geophys. Res.*, *99*, 999–1017, 1994.

Rasch, P. J., B. A. Boville, and G. P. Brasseur, A three-dimensional general circulation model with coupled chemistry for the middle atmosphere, *J. Geophys. Res.*, *100*, 9041–9071, 1995.

Russell, G., and J. Lerner, A new finite differencing scheme for the tracer transport equation, *J. Appl. Meteorol.*, *20*, 1483–1498, 1981.

Sausen, R., et al., The impact of NO_x emissions from aircraft upon the atmosphere at flight altitudes 8–15 km, in *AERONOX*, edited by U. Schumann, Comm. of the Eur. Communities contract EV5V-CT91-0044, Deutsche Luft-und Raumfahrt, Wessling, Germany, 1995.

Shimazaki, T., and A. R. Laird, A model calculation of the diurnal variations of minor constituents in the mesosphere and lower thermosphere including transport effects, *J. Geophys. Res.*, *75*, 3221–3235, 1970.

Solomon, S., R. R. Garcia, F. S. Roland, and D. J. Wuebbles, On the depletion of Antarctic ozone, *Nature*, *321*, 755–758, 1986.

Stolarski, R. S., et al., 1995 scientific assessment of the atmospheric effect of stratospheric aircraft, *NASA Ref. Publ.*, *1381*, 1995.

Tabazadeh, A., O. B. Toon, and E. Jensen, Formation and implications of ice particle nucleation in the stratosphere, *Geophys. Res. Lett.*, *24*, 2007–2010, 1997.

Thomason, L. W., L. R. Poole, and T. Deshler, A global climatology of stratospheric aerosol surface area density deduced from Stratospheric Aerosol and Gas Experiment II measurements: 1984–1994, *J. Geophys. Res.*, *102*, 8967–8976, 1997.

Thompson, A. M., R. R. Friedl, and H. L. Wesoky, Atmospheric

effects of aviation: First report of the Subsonic Assessment Project, *NASA Ref. Publ.*, *1386*, 1996.

Weaver, C. J., A. R. Douglass, and R. B. Rood, Tracer transport for realistic aircraft emission scenarios calculated using a three-dimensional model, *J. Geophys. Res.*, *100*, 5203–5214, 1995.

Weaver, C. J., A. R. Douglass, and D. B. Considine, A 5-year simulation of supersonic aircraft emission transport using a three-dimensional model, *J. Geophys. Res.*, *101*, 20,975–20,984, 1996.

World Meteorological Organization (WMO), Scientific assessment of ozone depletion: 1994, *Rep. 37*, Global Ozone Res. and Monit. Proj., Geneva, 1994.

World Meteorological Organization (WMO), Scientific assessment of ozone depletion: 1998, *Rep. 44*, Global Res. and Monit. Proj., Geneva, 1999.

D. Bergmann, P. S. Connell, D. Proctor, D. A. Rotman, and J. R. Tannahill, Lawrence Livermore National Laboratory, Mail Stop Li-103, Livermore, CA 94550. (drotman@llnl.gov)

D. B. Considine, Department of Meteorology, University of Maryland, College Park, MD 20742.

S. R. Kawa, S. J. Lin, and R. B. Rood, NASA Goddard Space Flight Center, Greenbelt, MD 20771-0001.

D. E. Kinnison and P. J. Rasch, National Center for Atmospheric Research, Boulder, CO 80307.

M. J. Prather, Department of Earth System Science, University of California at Irvine, Irvine, CA 92697-3100.

R. Ramaroson, Office National d'Etudes et Recherches Aerospatiales, 92322 Chatillon, France.

J. M. Rodriguez, Department of Marine and Atmospheric Chemistry, University of Miami, Miami, FL 33149-1098.

(Received May 3, 2000; revised July 31, 2000; accepted August 2, 2000.)